Revision 1

Crystallization of spinel from co-existing silicate and sulfide immiscible liquids: an equilibrium case with postcumulus reactions

Ya-Jing Mao[a*], Stephen J. Barnes[b], Louise Schoneveld[b], Belinda Godel[b], Morgan Williams[b], Dongmei Tang[a], Zhen Kang[a,c], Ke-Zhang Qin[a,c]

[a] Key Laboratory of Mineral Resources, Institute of Geology and Geophysics, Chinese Academy of Sciences (CAS), Beijing 100029, China

[b] Mineral Resources, Commonwealth Scientific and Industrial Research Organisation (CSIRO), Perth, WA6151, Australia

[c] College of Earth and Planetary Sciences, University of Chinese Academy of Sciences, Beijing 100049, China

[*]-corresponding authors: Ya-Jing Mao, maoyajing@mail.iggcas.ac.cn

Prepared for *American Mineralogist*

Word Count：~9800 words

Abstract

Spinel minerals occur as inclusions in both silicates and sulfides in the Kalatongke magmatic Ni-Cu deposit in NW China, showing textural and compositional variations. The spinel enclosed in olivine and other silicates (orthopyroxene, clinopyroxene, and hornblende) is predominantly Cr-magnetite with minor Cr-spinel, having wide variations in MgO (0.1-8.0 wt%), Al_2O_3 (1-25 wt%), Cr_2O_3 (3-20 wt%), and TiO_2 (0.5-6.2 wt%) contents. Such continuous variations suggest that Cr-magnetite in silicates was crystallized from residual melts and experienced extensive reaction with trapped liquid undergoing a typical tholeiitic trend of increasing Fe and Ti concentrations. Crystals of Cr-magnetite enclosed in disseminated sulfides have similar Mg, Al, Cr, Ti, V, Sc, Ga, Mo, Zr, and Nb concentrations to the Cr- magnetite in silicates. Such compositional similarity, which is explained by the simultaneous equilibrium crystallization of Cr-magnetite from the silicate and sulfide melts, shows that the Kalatongke deposit is a typical example of where the same mineral phase is formed from two co-existing immiscible liquids. However, the Cr-magnetite in disseminated sulfide and that in silicates show distinctly different crystal size distribution patterns, illustrating that the chemical equilibrium was attained despite contrasting growth rates, probably via diffusion. Nevertheless, the Cr-magnetite in disseminated sulfides shows significantly lower Ni, Co, and Zn contents (median value of 845, 22, 319 ppm) than that in silicates (median value of 1428, 160, 1039 ppm). This cannot be the result of sulfide fractionation because there is little compositional variation between Cr-magnetite included in pyrrhotite (early crystallized phase) and that immersed in chalcopyrite (late crystallized phase). Such Ni, Co, and Zn depletions, combined with the relatively constrained Fe/Ni, Fe/Co, and Fe/Zn ratios in those Cr-magnetite, are attributed to postcumulus reactions between Cr-magnetite and sulfide melts. The spinel hosted by massive sulfides is magnetite, which has distinctly different compositional variations and crystal size distribution patterns compared with those of the silicate-hosted Cr-magnetite, although the magnetite in massive ore generally has similar contents in some lithophile elements (Zr, Ta, Mo, Sn, Mn) to the silicate-hosted Cr-magnetite. This could be taken as evidence for a mixture of early accumulated sulfide pools with a component of drained sulfide from the cumulates above. This study shows a detailed textural and compositional investigation of spinel is useful to decode the sulfide evolution processes during the formation of magmatic Ni-Cu deposits and highlights that equilibrium crystallization and postcumulus reactions play critical roles in controlling the spinel/magnetite composition.

Keywords: Spinel, Magnetite, Equilibrium crystallization, Postcumulus reactions, Immiscible liquids, Kalatongke, Magmatic Ni-Cu deposit

Introduction

Spinel (*sensu latu*) in the form of chromite and chromite spinel (Cr-spinel) is commonly the first mineral phase on the liquidus of basaltic magmas and crystallizes over a wide range of conditions (e.g. Irvine, 1965; Dick and Bullen, 1984; Roeder, 1994; Barnes and Roeder, 2001). Its compositional variability has been widely used to constrain magma composition and evolution (e.g. Maurel and Maurel, 1982; Dick and Bullen, 1984; Sack and Ghiorso, 1991; Mao et al., 2015; Song et al., 2020), geotectonic settings (e.g. Dick and Bullen, 1984; Arai, 1992; Cookenboo et al., 1997; Barnes and Roeder, 2001), and magma oxygen fugacity (Hill and Roeder, 1974; O'Neill and Wall, 1987; J. Wood and Virgo, 1989). Accordingly, spinel has been widely used to trace the magmatic processes of intrusive rocks that host Ni-Cu mineralization (e.g. Frost and Groves, 1989; Barnes and Tang, 1999; Barnes and Kunilov, 2000; Dare et al., 2012; Evans, 2017; Schoneveld et al., 2020; Song et al., 2020; Taranovic et al., 2021). For magmatic Ni-Cu deposits, diffusive equilibrium between spinel, trapped liquid, and neighboring mineral phases are essential factors that control the final composition of the spinel (Irvine, 1965; Irvine, 1967; Jackson, 1969; Lehmann, 1983; Roeder and Campbell, 1985; Barnes, 1986) and must be taken into account in petrogenic interpretation. Crystal size distributions (CSD) of minerals can provide valuable information on growth rate and nucleation and thus have been widely used as a method of determining mineral crystallization kinetics in magmatic systems (Cashman and Marsh, 1988; Marsh, 1988; Higgins, 2002; Higgins, 2006). Though less attention has been paid to the CSD patterns of spinel (Giuliani et al., 2020), it has been demonstrated clearly that the morphology of spinel crystals is a distinctive indicator of crystallization mechanisms (Godel et al., 2013a).

Spinel in the form of magnetite is an important phase that can crystallize directly from sulfide liquid (Naldrett, 1969; Dare et al., 2012), making it a valuable indicator mineral in exploring magmatic Ni–Cu–PGE sulfide deposits (Boutroy et al., 2014; Dare et al., 2014; Ward et al., 2018; Moilanen et al., 2020). It has been shown that the composition of the sulfide liquid changes during fractional crystallization (Naldrett, 1969), and magnetite chemistry records that process (Dare et al., 2012; Boutroy et al., 2014; Duran et al., 2020). Generally, magnetite that crystallized early from sulfide liquid, along with monosulfide solution, is enriched in lithophile elements relative to that crystallized late in association with the intermediate sulfide solution, due to the relative compatibility of the more lithophile elements in the magnetite (Dare et al., 2012; Boutroy et al., 2014; Duran et al., 2020; Schoneveld et al., 2020). However, as pointed out by Dare et al. (2012), several other factors may control compositional variation in magnetite: concentration of the elements in the host silicate liquid, rate of cooling of the system, timing of the crystallization of magnetite from the sulfide liquid, and sub-solidus equilibrium. Notably, previous studies predominantly concentrated on magnetite compositional evolution of magnetite in massive sulfides (Dare et al., 2012; Boutroy et al., 2014; Ward et al., 2018; Jiao et al., 2019; Duran et al., 2020; Schoneveld et al., 2020), and there are few works on the compositional variations in magnetite associated with disseminated sulfides (Gao et al., 2013). The key factors controlling the variation in trace elements of magnetite from disseminated sulfides are unclear. In addition, magnetite composition is related to the silicate magma in the case of equilibrium crystallization as noted in the komatiite-hosted Ni-Cu deposits at Kambalda (Frost and Groves, 1989). The equilibration process and the interaction between spinel/magnetite and two immiscible liquids (silicate and sulfide liquids) remain less well known.

The NW China Kalatongke deposit is one of the several Permian magmatic Ni-Cu deposits in the Central Asian Orogenic Belt (e.g. Mao et al., 2008; Qin et al., 2011; Mao et al., 2018). The deposit is associated with mafic rocks and distinctive in having a high proportion of magnetite in sulfides (both massive and disseminated sulfides) as well as ubiquitous Cr-spinel (and Cr-magnetite) inclusions in silicate phases (Wang and Zhao, 1991; Song and Li, 2009; Zhang et al., 2009; Gao et al., 2012; Gao and Zhou, 2013; Wei et al., 2019; Kang et al., 2020; Mao et al., 2022a). It provides an ideal natural system to study the key controlling factors in the composition of Cr-spinel/magnetite enclosed in silicates and sulfides from disseminated to massive ores of magmatic Ni-Cu deposits. This study investigates the CSDs, integrated with major and trace element compositional variations in the Kalatongke spinel/magnetite to better understand the spinel crystallization mechanism and factors that control their compositional variation during the forming of magmatic Ni-Cu deposits. The findings have several implications for applying spinel compositions to understanding sulfide enrichment and fractionation processes in magmatic Ni-Cu deposits.

Geological background of the Kalatongke deposit and sample descriptions

The Central Asian Orogenic Belt is one of the biggest accretionary orogens, which grew southward from Siberia to the Tarim-North China cratons (Fig. 1) (e.g. Sengör et al., 1993; Xiao et al., 2008). The Kalatongke deposit in the center of the Central Asian Orogenic Belt in NW China is located approximately 20 km south of the Irtysh Fault (Fig. 1), which separates the Chinese Altay orogenic belt to the north and the East Junggar terrane to the south (Briggs et al., 2007). The Altai Orogenic Belt in China is mainly composed of Paleozoic volcanic and sedimentary rocks, abundant granitoids, and intermediate to mafic plutons (BGMRXUAR, 1993), reflecting a Middle Cambrian to Early Permian magmatic arc or components of an active marginal sequence (Xiao et al., 2008). The East Junggar terrane is composed of the Devonian to Carboniferous marine volcanic rocks intercalated with sedimentary rocks, two highly deformed and dismembered belts of ophiolites (the Zhaheba and Armantai ophiolites), and the Permian intermediate volcanics (BGMRXUAR, 1993). It is suggested that the East Junggar terrane was generated by Paleozoic northward subduction-accretion processes (Xiao et al., 2008). The Permian Kalatongke deposit is the largest accumulation of Ni-Cu mineralization in the Altay and East Junggar orogenic belts, whereas a dozen Ni-Cu deposits occur at the south margin of the Central Asian Orogenic Belt, e.g. the Huangshandong, Huangshanxi, Huangshannan, Baishiquan, Tianyu, Tulaergen, Poyi, and Poshi deposits (Mao et al., 2008; Qin et al., 2011; Xue et al., 2016). Among all these deposits, the Kalatongke deposit is the third largest magmatic Ni deposit with known resources of 33 million metric tons, grading

0.8 wt % Ni, 1.4 wt % Cu, and ~0.027 wt % Co (Wang and Zhao, 1991; Gao et al., 2012; Lu et al., 2019). The Kalatongke sulfide is characterized by a high Cu/Ni ratio (>1) compared to those from other regional deposits.

At least ten small mafic intrusions are present in the Kalatongke district (Fig. 2a). These intrusions are of the Permian age and intrude into the Devonian to Carboniferous volcanic and sedimentary rocks. These intrusions are distributed parallel to the north-west trending faults, commonly at the intersections of northwest-trending faults with west-northwest trending faults. Economic mineralization is mainly associated with the Permian Y1, Y2, Y3, and Y9 intrusions, with the Y1 and Y2 intrusions hosting more than 80% of the resource. The funnel-shaped Y1 intrusion is composed of olivine norite, gabbronorite, diorite, hosting net-textured to massive sulfide mineralization in the lower part of the intrusion (Fig. 2b). The tabular-shaped Y2 and Y3 intrusions are dominated by gabbronorite and diorite, hosting net-textured to disseminated mineralization at the bottom of each intrusion (Fig. 2c, d). Some of the massive to net-textured ore occurs as irregular and vein shapes in the wall rock between the Y1 and Y2 intrusions (Fig. 2d). Detailed descriptions of the Kalatongke deposit can be found in several recent publications (Qian et al., 2009; Song and Li, 2009; Zhang et al., 2009; Gao et al., 2012; Li et al., 2012; Gao and Zhou, 2013; Duan et al., 2017).

Samples used in this study were collected from the Y1 and Y2 intrusions as well as the orebodies between the two intrusions (Fig. 2b-d). There is a certain degree of sulfide fractionation at the hand-sample scale but no significant zoning at the orebody scale. This study chose 6 samples of olivine gabbronorite with disseminated to net-textured sulfides with little zoning for textural and compositional study on spinel. The olivine in these samples has Fo values of ~80 mol%, which is relatively primitive in the Kalatongke deposit (75-82 mol%) but relatively evolved compared to those of other Central Asian Orogenic Belt deposits (Fo80-90) (Mao et al., 2018; Lu et al., 2019; Barnes et al., 2022; Mao et al., 2022b). The relatively evolved olivine composition has been attributed to postcumulus trapped liquid reactions (Li et al., 2012). The disseminated and net-textured sulfides in these samples were formed by sulfide percolation and coalescences in the cumulus stage (Mao et al., 2022a). The magnetite in massive ore has been chosen for comparison (2 samples). The massive sulfides occur as 2-3-meter-wide veins and cross-cutting the host intrusion with Ni/Cu ratios comparable to the disseminated ores. A detailed textural study of these samples was reported in Mao et al. (2022a).

Analytical methods

Crystal size distribution of spinel

Samples with regular to granular spinel grains were selected for CSD calculation, whereas the massive sulfide sample with dendritic magnetite grains (Fig. 3d) was excluded from size statistics. Crystals of spinel were segmented from other phases using Adobe Photoshop based on the high-resolution thin-section images, following the method of Godel et al. (2013b) and Mao et al. (2018). Subsequently, the touching magnetite crystals occurring as clusters were separated manually, shown in the processed high-resolution images (Supplementary Materials 1 and 2). The images of segmented Cr-magnetite/magnetite grains were subsequently measured using ImageJ for their morphology and size information, such as area, length, width, fit ellipse, etc. The equivalent circle diameter (ECD, i.e. the diameter of a circle having the same area as the crystal), is calculated to describe the size variation of the spinel. These results were loaded into CSDCorrections (Version 1.6, Higgins, 2006) for CSD calculation. Short : Inter : Long of 1:1:1, roundness of 0, and 5 bins per decade (2.51, 3.98, 6.31, 10, 15.8, 25.1, 39.8, 63.1, 100, 158, 251 μm) were used for stereoscopic correction. The CSD is expressed as a plot of population density [n, actually ln (n)] in units of numbers of crystals per volume per unit length of the bin size (i.e. n mm^{-4}), versus crystal length (mm). The segregation of touching grains is based on Cr-magnetite/magnetite morphology using high-resolution optical images; the segregation of some clusters, especially the irregular shaped magnetite in massive ore, was in some cases somewhat arbitrary. The accuracy of phase segmentation was verified using either X-ray fluorescence analysis (Mao et al., 2018) or scanning electron microscopy conducted at CSIRO, Perth (Fig. 3).

Major and trace element concentration analysis

The Cr-spinel, Cr-magnetite, and magnetite composition were analyzed by electron microprobe analyzer (EMPA) for major elements and subsequently by laser ablation Inductively Coupled Plasma Mass Spectrometry (LA-ICP-MS) for trace elements on the same spots. The EMPA was conducted at the Institute of Geology and Geophysics, Chinese Academy of Sciences, using a JEOL JXA8100 electron probe. The operating conditions were 15 kV accelerating voltage, 12 nA beam current, 5 μm beam size, and 30 seconds peak counting time. International oxide and silicate standards were used for calibration. The ferric iron content of each analysis of Cr-magnetite and magnetite was calculated based on the assumption of stoichiometry using the EMPA data. It was assumed that the Cr-magnetite was of the ideal XY_2O_4 formula, where X = (Fe^{2+}, Mg, Ni, Mn, Co, Zn) and Y = (Cr^{3+}, Al^{3+}, Fe^{3+}). This method may generate large relative errors for the Fe^{3+} (Barnes and Roeder, 2001); thus, relatively small variations and differences in ferric iron content of the sample were neglected.

The LA-ICP-MS analyses of Cr-spinel and Cr-magnetite were collected at CSIRO using a Photon Machines, ATLex 300si-x Excite 193-nm Excimer ArF laser with samples in a double volume Helix-II sample cell attached to an Agilent 7700 ICP-MS. The plasma conditions were optimized daily to obtain the highest counts with oxide production ($^{248}ThO/^{232}Th$) remaining below 0.4. The laser was set to a repetition rate of 9 Hz and a 50 μm spot. The data consists of 30 seconds of the background at the start of each analysis before 260 shots of a sample (~30 s). The He carrier gas was set at 0.6 L/min in both the cup and cell (1.2 L/min total). The carrier gas was subsequently mixed with 0.8 L/min of Ar in a Meinhard mixing chamber. The certified reference material for the oxide analysis was U.S. Geological Survey standard GSD-2G with an internal standard element of Fe. The Fe content from EMPA for the same grain was used as the internal standard value. The BCR-2G and MASS-1 were used as secondary standards to corroborate the accuracy and reproducibility of the analyses (see Appendix Fig. 1, Supplementary Material 3). The isotopes measured in this routine were: Mg^{25}, Al^{27}, Si^{29}, S^{34}, Ca^{43}, Sc^{45}, Ti^{49}, V^{51}, Cr^{53}, Mn^{55}, Fe^{57}, Co^{59}, Ni^{61}, Cu^{63}, Cu^{65}, Zn^{66}, Ga^{71}, Ge^{74}, Y^{89}, Zr^{90}, Nb^{93}, Mo^{95}, Ru^{99}, Ru^{101}, Rh^{103}, Pd^{105}, Ag^{107}, Pd^{108}, Cd^{111}, In^{115}, Sn^{118}, La^{139}, Yb^{172}, Hf^{178}, Ta^{181}, W^{182}, Os^{192}, Ir^{193}, Pt^{195}, Au^{197}, Pb^{208}. The argide interferences on the platinum group elements were monitored and corrected in the raw data by measuring Cu, Co, and Ni metals. The platinum group elements contents of samples were all below the detection limits (~40 ppb). Blocks of standards were measured at the beginning and end of the run, as well as between every 10 to 15 unknown analyses. Data were reduced using Iolite software (version 3.63; Paton et al., 2011). The trace element analyses of magnetite were conducted by LA-ICP-MS at the Wuhan SampleSolution Analytical Technology Co., Ltd., Wuhan, China. Laser sampling was performed using a GeolasHD laser ablation system with spot size and frequency of 9 Hz and 50 μm, respectively. The isotopes measured at Wuhan include those analyzed at CSIRO except the platinum group elements. Helium was applied as a carrier gas. Argon was used as the make-up gas and mixed with the carrier gas via a T-connector before entering the 7700e ICP-MS. The primary standard is the U.S. Geological Survey standard GSD-2G, with Fe used ash an internal standard. The Fe content from EMPA for the same grain was used as the internal standard value. The BCR-2G, BHVO-2G, and BIR-1G were analyzed as secondary standards followed by every 10 analyses of samples. Each analysis incorporated a 20-30 seconds background acquisition before 50 seconds of data acquisition. An Excel-based software ICPMSDataCal was used to perform off-line selection and integration of background and analyzed signals, time-drift correction, and quantitative calibration for the trace element analysis (Liu et al., 2008). The accuracy and reproducibility of the analyses are included in Appendix Fig. 1 (Supplementary Material 3). A Python package, ‘pyrolite’, was used to process and visualize the geochemical data (Williams et al., 2020).

Results

Classification of the spinel in the Kalatongke deposit

Based on the occurrence, crystal size variation, and chemical composition (shown below), the spinel of the Kalatongke deposit can be classified into four groups (Fig. 3):

1. Cr-spinel in olivine (strictly some of these are Cr-magnetite, but Cr-spinel is used to distinguish it from that in other silicates),
2. Cr-magnetite in other silicates (orthopyroxene, clinopyroxene, hornblende),
3. Cr-magnetite in disseminated sulfides, and
4. Magnetite in massive sulfides, further classified as Cr-magnetite/magnetite in pyrrhotite and in chalcopyrite.

The spinels from the four groups show a large variation in grain size, as quantified by the equivalent circle diameter (ECD) (Fig. 4). The Cr-spinel in olivine has a euhedral to rounded shape (Fig. 3a, b, d), with a maximum ECD less than 100 μm, mostly less than 50 μm. The grain diameters of the Cr-magnetite included in other silicates (ECD varying from 10 to 100 μm, Fig. 3a, b, d) tend to be slightly larger than those included in olivine, but some grains can have ECD larger than 200 μm. On the other hand, Cr-magnetite enclosed in disseminated sulfides occurs as equant grains located close to, but not on, the edge of the sulfide blebs (Fig. 3d). The Cr-magnetite in disseminated sulfide tends to be more irregular and coarser than those included in silicates (Fig. 3e). The magnetite included in massive sulfides is coarse-grained (Fig. 3c). Some grains have ECD larger than 2 mm (Fig. 3c, f). Most of the magnetite in massive ore is euhedral, but irregular to dendritic-shaped grains have been observed from some massive ores (Fig. 3c, d). A minor amount of ilmenite occurs as exsolution lamellae in grains of Cr-magnetite/magnetite from the disseminated and massive ores.

Crystal size distribution patterns

For simplicity, the Cr-spinel in olivine and the Cr-magnetite in other silicates are combined as Cr-magnetite in silicates for CSD measurement. The populations of Cr-magnetite grains in silicates, disseminated sulfides, and magnetite grains in massive sulfides show distinct log-linear CSDs, defining three types of log-linear distributions (Fig. 4). A single crystallization event should be defined by a single linear slope in log space on the CSD plot and the intercept representing the nucleation density of the mineral (Marsh, 1988). The characteristic length is estimated using the negative inverse of the slope (-1/slope) and is equal to the residence time multiplied by the growth rate (Marsh, 1988).

The CSDs exhibit variable intercepts and slopes. The CSD of Cr-magnetite in silicates yields a high intercept and a steep slope. The CSD of Cr-magnetite grains included in disseminated sulfides has a lower intercept and a gentler slope compared to that of Cr-magnetite grains in silicates. The CSD of magnetite grains included in massive sulfides shows the lowest intercept and the gentlest slope. The nucleation density decreases from $3*10^{-2}$ to $2*10^{-3}$ nuclei/mm^3 from Cr-magnetite in silicates to Cr-magnetite in disseminated sulfide. The magnetite in massive ore has the lowest nucleation density ($5*10^{-5}$ nuclei/mm^3). The characteristic length increases from 23.4 mm for Cr-magnetite in silicates to 54.8 mm for Cr-magnetite in sulfide. The magnetite in massive sulfide has the largest characteristic length of 165.9 mm.

Major element variations in spinel

The spinel enclosed in olivine and other silicates (orthopyroxene, clinopyroxene, and hornblende) is dominantly Cr-magnetite with minor Cr-spinel, having wide variation in MgO (0.1-7.6 wt%), FeO (40-90 wt%), TiO_2 (0.1-6.3 wt%), MnO (0.2-1.8 wt%), Al_2O_3 (1.0-25.5 wt%), Cr_2O_3 (3.0-20.5 wt%) contents, and Mg# values ($100*Mg/[Mg+Fe^{2+}]$, ~0-40 mol%) (Supplementary Material 3, Fig. 5a-e). The content of major elements of Cr-magnetite inclusions in the disseminated sulfides overlaps with that of the Cr-magnetite included in silicates, but with lower MgO (0.1-2.0 wt%), Al_2O_3 (0.1-3.0 wt%), and Cr_2O_3 (0.1-8.5 wt%) contents and Mg# values (~0-17 mol%). The Cr-magnetite in both silicates and disseminated sulfide have the same variations in TiO_2 and MnO concentrations (Fig. 5b, c). The Cr# value (defined as $100*Cr/[Cr+Al]$) of the Cr-magnetite included in disseminated sulfide varies from 60 to 80 mol%, whereas that of the Cr-magnetite in silicates varies from 35 to 90 mol% (Fig. 5f). The spinel hosted by massive sulfide is magnetite (FeO > 90 wt%), which has almost no Al_2O_3 and Cr_2O_3 (Fig. 5a, d, e). The TiO_2 in magnetite (0-0.5 wt%) is significantly lower than that in the Cr-magnetite (0.1-6.3 wt%) (Fig.

5b). The MnO content in magnetite (0.5-1.1 wt%) is comparable to that in the Cr-magnetite (0.2-1.3 wt%; Fig. 5c).

Spinel compositions from regional Huangshandong, Huangshanxi, Huangshannan, and Xiangshan deposits in the Central Asian Orogenic Belt are included for comparison (Mao et al., 2014; Mao et al., 2015; Xue et al., 2016). The spinel of the Kalatongke deposit, representing the Cr-spinel and Cr-magnetite in both silicates and disseminated sulfides, is enriched in FeO, TiO_2, MnO, and depleted in MgO, Al_2O_3, and Cr_2O_3 contents compared to the Cr-spinel hosted in silicates from regional Ni-Cu deposits (Fig. 5). The variations in Cr# and Mg# values of the Kalatongke spinel are wider (Fig. 5f). Specifically, the Kalatongke spinel has higher Cr# (30-90 mol%, commonly >60 mol%) and lower Mg# values (0-40 mol%, commonly <20 mol%) compared to spinel from other regional deposits (Cr#: 30-60 mol%, Mg#: 20-60 mol%, Fig. 5f). The Mg# values in the Kalatongke spinel are lower than those in other deposits, consistent with olivine being more evolved in the Kalatongke deposit than in the other deposits (Mao et al., 2022b). The regional Ni-Cu deposits show a trend of widely variable Cr# at high Mg# and low Fe^{3+} content, consistent with the Cr-Al trend defined by Barnes and Roeder (2001), to which some of the Kalatongke Cr-spinel is similar (Fig. 5f, 6). In contrast, most of the Kalatongke Cr-magnetite is more comparable with the Fe-Ti trend (Barnes and Roeder, 2001), in which the Fe^{3+} and TiO_2 content increase at constant Cr# (Fig. 6). Thus, the Cr-spinel (Cr-magnetite) of the Kalatongke deposit illustrates a compositional trend that is a combination of Cr-Al and Fe-Ti trends (Fig. 6). For Cr-magnetite included in disseminated sulfides, the Fe^{3+}

contents overlap with that of Cr-magnetite enclosed in olivine and form a continuum with some of the Cr-magnetite in other silicates (Fig. 6). Such a continuous trend of Cr-magnetite in silicates and Cr-magnetite in disseminated sulfides is seen from the variation in Mg#, Cr#, Al_2O_3, Cr_2O_3, TiO_2 contents (Fig. 5).

Trace element variations in spinel

The Cr-magnetite grains in both silicates and disseminated sulfides have similar V, Sc, and Ga, Mo, Zr, Nb contents (Supplementary Material 3, Fig. 7 a-f). The V and Sc contents of two Cr-magnetite populations vary from 1000 to 3000 ppm, and from 0.5-9.6 ppm, respectively. These Cr-magnetite crystals have 30-88 ppm Ga, 0.1-5.2 ppm Mo, ~0.1-25.4 ppm Zr, and <0.1-2.9 ppm Nb. The V and Ga abundances in Cr-magnetite from disseminated sulfide are lower than but overlap with those of Cr-magnetite from silicates (Fig. 7a, c). On the other hand, the Ni, Zn, and Co contents of magnetite in disseminated sulfides are significantly different from those included in silicates (Fig. 7 g-i, 8). The Cr-magnetite in disseminated sulfides shows overall lower Ni, Co, and Zn contents (Ni, Co, and Zn median value of 845, 22, 319 ppm) compared to those included in silicate minerals (Ni, Co, and Zn median value of 1428, 160, 1039 ppm). Importantly, the Ni, Co, and Zn contents are relatively scattered, and the Co and Zn decrease with the increasing Fe^{2+} (atom per formula unit, apfu) in the Cr-magnetite in silicates. In contrast, those values change little for the Cr-magnetite included in the disseminated sulfides (Fig. 8). The Fe/Ni ratio of Cr-magnetite in disseminated sulfide is relatively constant with increasing Fe^{2+} apfu, whereas Fe/Co and Fe/Zn show small but consistent linear increases with Fe^{2+} apfu

(Fig. 8 b, d, f).

For Cr-magnetite in disseminated sulfides, there is no detectable compositional difference between Cr-magnetite inclusions in pyrrhotite and those in chalcopyrite (Fig. 5, 7, 9). For instance, the Cr-magnetite in pyrrhotite of disseminated sulfides has Ni contents that vary from 476 to 1575 ppm (median value of 838 ppm), Co contents vary from 4.4 to 71.7 ppm (median value of 21.8 ppm), and Zn contents range from 141 to 1028 ppm (median value of 347 ppm), whereas the Cr-magnetite in chalcopyrite of disseminated sulfides has Ni contents that vary from 588 to 1403 ppm (median value of 868 ppm), Co contents that range from 4.3 to 48.2 ppm (median value of 24.6 ppm), Zn contents that vary from 144 to 745 ppm (median value of 280 ppm).

The trace element composition variations of magnetite included in massive sulfides are distinct from those of Cr-magnetite in silicates and disseminated sulfides (Fig. 7, 8, 9). The V, Sc, and Ga contents are much lower in magnetite than those in Cr-magnetite (Fig. 7a-c), but the Co, Mo, and Zr contents in magnetite are comparable to those in Cr-magnetite (Fig. 7e, g, h). The Ni content in magnetite is lower than that in Cr-magnetite from silicates but higher than that in Cr-magnetite from disseminated sulfides (Fig. 7d). Moreover, the V, Co, and Zn contents in magnetite included in pyrrhotite are lower than those included in the chalcopyrite (Fig. 7a, h, i). The Fe/Ni, Fe/Co, and Fe/Zn ratio in the magnetite included in pyrrhotite is generally higher than those included in chalcopyrite (Fig. 8b, d, f). Although the content of several elements (Al, Sc, Ga, Mg, Ti, V) in the magnetite is much lower than the Cr-magnetite, some elements (Si, Zr, Ta, Mo, Sn, Mn) show comparable crust-normalized patterns (Fig. 9c).

In the discrimination diagram of magnetite in massive sulfide (Fig. 10, Dare et al., 2012), the magnetite included in the massive sulfide of the Kalatongke plots in the field associated with evolved Fe-rich sulfide, whereas the Cr-magnetite in silicates and disseminated sulfides plot close to the field related to primitive Fe-rich sulfide with lower Ti, V, and higher Ni contents. The former relationship shows the vein-type massive sulfide has experienced a certain degree of sulfide fractionation, whereas the latter is consistent with the observation that these disseminated sulfides appear as droplets-networks without significant differentiation into monosulfide solution and intermediate sulfide solution. The lower Ti content in the Cr-magnetite than that of magnetite associated with primitive Fe-rich sulfides from the Huangshandong and Sudbury deposits (Fig. 10a) suggests that the Kalatongke system is relatively depleted in Ti, which could be used to explain the rareness of ilmenite exsolution in the Kalatongke Cr-magnetite (Fig. 3e).

Discussion

Protracted crystallization of Cr-spinel (Cr-magnetite) from the basaltic magma

The occurrence of Cr-spinel (Cr-magnetite) inclusions in olivine, pyroxene, and other silicates (Fig. 3) is comparable to that of other deposits in the Central Asian Orogenic Belt (Mao et al., 2014; Mao et al., 2015; Xue et al., 2016), but with distinct compositional trends (Fig. 5, 6). The variation in Cr^{3+}-Al^{3+}-Fe^{3+} cations of the

Kalatongke Cr-spinel (Cr-magnetite) is more comparable to those observed at the Noril'sk-Talnakh deposits, a feature that has been attributed to continuous Cr-spinel crystallization and interaction with evolving trapped liquid (Barnes and Kunilov, 2000; Schoneveld et al., 2020). The Fe-Ti trend thus records the entire solidification process from liquidus to solidus at the Noril'sk-Talnakh deposit (Schoneveld et al., 2020). The occurrence of Cr-spinel (Cr-magnetite) inclusions in various silicate minerals (Fig. 3), together with the gradual Mg-Fe-Cr-Al variations (Fig. 5, 6), suggest that the Kalatongke Cr-spinel (Cr-magnetite) population crystallized from melts with continuously changing composition over a long period. Note there is a large compositional variation in Cr-spinel inclusions in olivine (Fig, 5, 6), which is comparable to that of the Cr-magnetite included in other silicates. This reflects either that the Cr-spinel in the olivine continued to react with the trapped liquid outside olivine (e.g. Roeder and Campbell, 1985), or the Cr-spinel continued to grow from the trapped liquid as it evolved and was subsequently captured by overgrowth olivine (Barnes and Kunilov, 2000; Schoneveld et al., 2020). Most likely, both factors played roles in the chemistry of Cr-spinel (Cr-magnetite) in olivine. The relatively larger size of Cr-magnetite within other silicates relative to the Cr-spinel in olivine shows that the Cr-spinel included in the olivine did not have a chance to grow into larger crystals, whereas the Cr-magnetite in other silicates had longer residence times in the magma crystallization range and hence more chance to interact with the evolved melts. The wide variety and overall high TiO_2 content (Fig. 5b) in the Cr-magnetite inclusions in silicates (except olivine) are likely the results of extensive reaction with evolving trapped liquid having increasing Fe and Ti concentrations. The extensive reaction may be enhanced by the hydrous nature of the interstitial melt (Kang et al., 2020), which remained partially molten to lower temperature, allowing a more extensive buildup of Fe and Ti in the late stages of fractionation.

Equilibrium crystallization of Cr-magnetite from sulfide and silicate melts

The concentrations of major and most trace elements of Cr-magnetite included in disseminated ore are comparable to those of Cr-magnetite included in silicate phases (Fig. 5, 6, 7), which is inconsistent with the findings of several studies that the chemistry of magnetite crystallized from sulfide is significantly different from those crystallized from silicate melt (Dare et al., 2012; Dare et al., 2014). Moreover, mechanical capture of Cr-magnetite crystallized from silicate melt by sulfide melt could be ruled out by the distinct CSD patterns of the magnetite and Cr-magnetite (Fig. 4).

Naldrett (1969) showed that sulfide liquids contain a substantial proportion of O, which increases as they crystallise to form solid sulfides. He noted the higher abundance of magnetite in massive relative to disseminated sulfides at Sudbury and proposed that oxygen diffuses from the disseminated ore to a large body of slowly-cooled silicate magma, driving magnetite nucleation and growth at the interface between sulfide and silicate melts, whereas massive sulfide pools tend to solidify as closed systems and reatin their original O contents. The experimental work of Fonseca et al. (2008) further shows that the oxygen abundance in natural magmatic sulfides was significantly lower than that which can be dissolved in the equivalent-mass sulfide melt, suggesting the loss of oxygen from the sulfide melt during solidification and the tendency of magnetite nucleation at the interface. This interface growth model explains the common distribution of Cr-magnetite close to the boundaries of disseminated sulfides from both the Kalatongke deposit (Fig. 3) and the Voisey's Bay deposit (Naldrett et al., 2000), as well as in many komatiite-hosted deposits such as Black Swan (Frost and Groves, 1989; Dowling et al., 2004), and accounts for the similarity in the chemistry of Cr-magnetite included in sulfide and silicates (e.g., Fig. 9, 10). However, according to the interface growth model, the domain where sulfide liquid touches early crystallized cumulus olivine would have much less magnetite than the domain where sulfide touches silicate melts (now hornblende and plagioclase), similar to the distribution of Cr-rich magnetite along komatiite xenoliths included in massive ore in komatiites (Frost and Groves, 1989; Fonseca et al., 2008). Such a distribution pattern is inconsistent with the observations from Kalatongke disseminated ores. We suggest that the Cr-magnetite of the Kalatongke disseminated ore was crystallized from the sulfide melt. The tendency of Cr-magnetite distributed close to the sulfide boundary could be explained by synchronous magnetite growth with the outward diffusion of oxygen from the sulfide melt to the silicate melt. Magnetite crystallization from disseminated sulfide agrees with the single stage of crystal growth revealed by the log-linear CSD distribution of Cr-magnetite (Fig. 4).

It is a well-established axiom in igneous petrology dating back to Bowen (1928) that two immiscible liquids in equilibrium with one another should also be in equilibrium with the same solid phase; Cr-magnetite crystallized from coexisting silicate and sulfide melts in equilibrium with one another should have the same composition, although in nature they rarely if ever do, even when in very close proximity (e.g. Frost and Groves, 1989), due to diffusion-limited disequilibrium. The similar composition (Fig. 5, 7, 9b) between the Cr-magnetite crystals in disseminated sulfides and the Cr-magnetite inclusions in silicates indicates that Kalatongke is an unusual case of where Cr-magnetite from the silicate and sulfide compositions conforms to the equilibrium case, or at least approaches it. Nevertheless, the discrete log-linear CSDs show that Cr-magnetite grains in silicates and those in disseminated sulfides crystallized with distinctly different nucleation density and growth rate (Fig. 4). The textural and grain size differences (Fig. 4) in Cr-magnetite in sulfide and that in silicate suggest that the chemical equilibrium may have been reached after crystallization via diffusive processes. On this evidence the disseminated sulfides formed in close enough diffusive connection with the parent silicate melt that all the essential Cr-magnetite components were able to approach equilibrium during the late stages of solidification where the Cr-magnetite were becoming Fe and Ti-rich during the reaction with trapped liquid.

The situation at Kalatongke is in contrast with that observed by Taranovic et al. (2021) at Nova-Bollinger Ni-Cu deposits in Western Australia, where two distinct spinels, an Al-Mg rich spinel s.s. and magnetite, coexist stably within adjacent silicate grains and sulfide liquid blebs respectively. This reflects the operation of the immiscibility gap within the spinel prism (Sack and Ghiorso, 1991) and arises from the growth of Al-Mg rich spinels from the silicate melt at the higher pressure of emplacement of Nova-Bollinger.

Postcumulus reactions between Cr-magnetite and sulfide melts

Although most of the elements in Cr-magnetite within sulfides and that within silicates exhibit an equilibrium signature, the depletions in Ni, Co, and Zn in Cr-magnetite in disseminated sulfide relative to those of Cr-magnetite in silicates (Fig. 8) show that additional processes exert control these chalcophile elements beyond only equilibrium crystallization. These depletions may be the result of synchronous crystallization of Cr-magnetite with monosulfide solid solution from the sulfide melt, during which these elements (Ni, Co, and Zn) partition strongly into the monosulfide solid solution (Dare et al., 2012). This is somewhat like the fractionation model observed from massive sulfide ore bodies (Fig. 10), which suggests that the Cr-magnetite was a record of the compositional change of sulfide melt. Specifically, the following geochemical signatures are expected for the crystallization model. Firstly, continuous variation of compatible elements (such as Cr, Al, Ni, etc.) in Cr-magnetite. Secondly, the magnetite records the changing composition of the fractionating sulfide liquid. The Ni content in early crystallized Cr-magnetite increases slightly or remains constant in the later crystallized magnetite (Fig. 10c) (Dare et al. 2012; Boutroy et al. 2014; Duran et al. 2020). Similarly, the Zn is enriched in the late Cu rich fractionated sulfide (Dare et al., 2012). Thirdly, a large variation in lithophile element (especially Cr, Al, V, Ti) abundances exists in Cr-magnetite crystallized at different stages, as these elements tend to be enriched in early Cr-magnetite phase crystallized with Fe-rich monosulfide solid solution (occurring as inclusions in pyrrhotite) and depleted in late formed phase crystallized from residual Cu-rich liquid (occurring as inclusions in chalcopyrite) (Dare et al., 2012). The uniform compositional variations of the Kalatongke Cr-magnetite enclosed in both pyrrhotite and chalcopyrite of the disseminated ore (Fig. 5, 7-9) are distinctly different from the fractionation model, conforming to the proposition that Cr-magnetite compositions were controlled by equilibrium crystallization and illustrate that the Ni-Co-Zn depletions in Cr-magnetite included in disseminated sulfide were not associated with sulfide fractionation.

Alternatively, we suggest that the Ni, Co, and Zn depletion in Cr-magnetite is a record of element exchange between Cr-magnetite and sulfide melt, i.e. re-equilibration due to postcumulus reactions. The exchange equilibria for element pairs between sulfide and coexisting olivine have been studied by extensive experimental measurements (e.g. Fleet and MacRae, 1988 and references therein; Brenan, 2003) and identified in numerous natural magmatic Ni-Cu systems, such as the Mirabela intrusion in Brazil (Barnes et al., 2011), the Betheno deposit in Western Australia (Barnes et al., 2013), and the deposits in NW China (Mao et al., 2018). For the olivine-sulfide system, it has been demonstrated that the exchange coefficient ($K_{D\ \text{olivine-sulfide}}$) for Fe and Ni is associated with oxygen fugacity, sulfur fugacity, Ni content in the sulfide melt, etc. (e.g. Fleet and MacRae, 1988; Brenan, 2003; Barnes et al., 2013). Comparatively, Fe/M ratios in Cr-magnetite, where M refers to Ni, Co, Zn and X_i is the mole fraction of component i in the phase of interest, may associate with the Fe/M ratio in sulfide and the $K_{D\ \text{Cr-magnetite-sulfide}}$:

$$K_{D\ sulfide/Cr-magnetite} = \left(X_{MS}/X_{FeS} \right)_{sulfide\ liquid} \Big/ \left(X_{MO}/X_{FeO} \right)_{Cr-magnetite}$$

Accordingly, the elemental exchange model can be tested by the Fe/M ratios in Cr-magnetite. Assuming the $K_{D\ \text{Cr-magnetite-sulfide}}$ remains constant and the change of Fe/M ratio in the Kalatongke sulfide is negligible, the variation in Fe/M ratio in Cr-magnetite should be relatively small. The restricted ratios of Fe/Ni (150 to 250) and Fe/Co (6000 to 8000) in Cr-magnetite in disseminated sulfide (Fig. 8b, d, f) suggest that the Ni and Co depletions in Cr-magnetite can be the result of exchange equilibrium between Cr-magnetite and sulfide. The alternative interpretation would be that these ratios in the disseminated ores are controlled by the equivalent exchange equilibria with olivine:

$$K_{D\ olivine/Cr-magnetite} = \left(X_{MO}/X_{FeO} \right)_{olivine} \Big/ \left(X_{MO}/X_{FeO} \right)_{Cr-magnetite}$$

However, it is significant that the M/Fe ratios in the massive sulfide-hosted magnetite are similar to those in the disseminated ores. This implies that divalent metal exchange with sulfide is the dominant control for magnetite from different ore types.

The Fe/Zn and Fe/Co ratios tend to increase slightly with the ferrous iron (Fe^{2+}) in Cr-magnetite, which may be explained by the Fe-Zn (Fe-Co) exchange reactions being relatively sensitive to either sulfide composition or conditions of the system. Temperature dependence of the Fe/Zn and Fe/Co K_D is the likely explanation. We note that the element exchange mechanism cannot be used to explain the lack of Ni, Co, and Zn depletion in the magnetite included in chalcopyrite from massive sulfide

(Fig. 8). Such inconsistency could be reconciled by the relatively lower temperature of the fractionated sulfide melt (low diffusive rate) together with the relatively fast-cooling rate (limited equilibrium time) in the massive sulfides. The explanation is consistent with the geological distribution of the Kalatongke massive ore, which commonly occurs as sulfide veins intruding into the fractures of the cooled intrusive body and/or cold wall rocks. The fast-cooling rate is suggested by the dendrite texture of the magnetite in massive sulfide (Fig. 3d). Nevertheless, the Fe, Ni, Co, and Zn exchange between Cr-magnetite and sulfide melt may remain active at late stages of sulfide fractionation within the intrusive body, suggesting that the postcumulus modification may have erased the fractionation signal in Cr-magnetite of most magmatic systems. Sub-solidus reactions between magnetite and sulfide minerals played a subtle role in the trace element compositions as there is little compositional difference between magnetite (also Cr-magnetite) enclosed in pyrrhotite and that included in chalcopyrite.

Potential application of spinel composition to sulfide enrichment processes

There is a much greater contrast in composition between disseminated sulfide-hosted Cr-magnetite and those found within massive sulfide, specifically in the much lower concentrations of the strong lithophile elements (Ti, Al, Cr, V, Sc, Ga, shown in Fig. 5, 7, 9) in the latter. This is more typical of the situation in magmatic sulfides: magnetite in the massive sulfide pools crystallized under conditions where there was limited diffusive equilibration with the parent silicate melt (Naldrett et al., 2000). In this light, we can consider whether the size distribution and composition of magnetite in sulfide could be used to indicate the origin of the massive ores. Massive ores could be formed either by sulfide accumulation from the magma prior to accumulation of the overlying cumulates, or by coalescence and percolation of sulfide through the silicate-sulfide-melt mush and drainage to the bottom (Barnes et al., 2017). For the latter case, extensive interdiffusion of elemental components between silicate and sulfide melts might be expected, leveling out the difference in the compositions of magnetite between the two sulfide types. In such a case, the ubiquitous distribution of magnetite in the massive sulfides, together with the wide compositional variation in magnetite from disseminated and massive ores (Fig. 10), could be taken to indicate that the massive ore of the Kalatongke deposit was not the result of the coalescence of interstitial disseminated sulfides. This would be further evidence that sulfide pools have formed early in the Kalatongke deposit, probably before the formation of disseminated ores. However, this is not a conclusive argument; it is even likely that magnetite saturation in the massive sulfide liquid could have occurred subsequent to percolation and drainage, from an evolved sulfide melt spatially and chemically isolated from the silicate magma. Under these circumstances, this magnetite would be expected to be strongly depleted in the lithophile components (Fig. 10). The massive sulfide magnetites here actually show somewhat transitional character, being generally similar to the disseminated and silicate hosted magnetites in some lithophile elements – Zr, Ta, Mo, Sn, and Mn – while being strongly depleted in others – Al, Sc, Mg, Ga, V, and Cr (Fig. 9c, 10). This could be taken as indicative evidence for a hybrid model: a mixture of early accumulated sulfide pools with a component of drained sulfide from the cumulates above.

Implications

The compositional comparison of Cr-magnetite and magnetite from different sulfide textures reveals that the Kalatongke deposit is an example of where the same mineral phase from two immiscible liquids exhibit approximately equivalent compositions (Bowen, 1928; Frost and Groves, 1989). Such a finding suggests that equilibrium crystallization may be an important process in generating the complex chemistry of Cr-magnetite/Cr-spinel in magmatic Ni-Cu deposits, particularly for the Cr-magnetite in disseminated sulfide which has the opportunity to interact with the coexisting silicate melts.

The equilibrium between Cr-magnetite in sulfide with the silicate liquid illustrates that the Cr-magnetite is a potential candidate to trace sulfide migration and percolation history. The slight enrichment in several trace elements (Zr, Ta, Mo, Sn, Mn) in magnetite from massive ore is inferred to be formed by the mixture of early accumulated sulfide pools with a component of drained sulfide from the cumulates. The present study suggests that the trace element component in spinel may serve as an indicator for not only the compositional evolution of silicate/sulfide melts (Dare et al., 2014; Duran et al., 2020; Schoneveld et al., 2020) but also the percolation and enrichment history of sulfide liquid.

The Kalatongke case study shows that the Cr-magnetite (magnetite) has experienced reactions with the coexisting sulfide melt at the postcumulus stage, generating outward Ni, Co, and Zn (divalent cation) migration to sulfide melt. The initial content of divalent cations in Cr-magnetite can only be preserved when the sulfide cools rapidly, such as in massive sulfide veins intruding into cold wall rocks. The element exchange with the coexisting sulfide melt may be the key factor for the chalcophile element concentration in Cr-magnetite/magnetite of magmatic Ni-Cu deposits, suggesting that fractional signatures of divalent cations in Cr-magnetite/magnetite may be completely overprinted by postcumulus reactions.

Acknowledgments

We acknowledge Yong Wang, Bin Wang, Lei Zhang, Zheng Zhu, Ayideng, Jianghua Shi, and Gang Ma et al. from the Xinxin corporation for their guidance during underground trips. Linru Fang and Shengchao Xue helped to collect samples. The LA-ICP-MS analysis at CSIRO was conducted within the National Geosequestration Laboratory in Kensington, WA. Hongfang Chen and Jiakang Kong assisted LA-ICP-MS analyses at the Wuhan SampleSolution. This work has been supported by the National Sciences Foundation of China (42072105, 41830430, 92162323), the National Key Research and Development Program of China (2017YFC0601204), and the Youth Innovation Promotion Association CAS. Felix Genske, Sarah Dare, and two anonymous reviewers are acknowledged for their detailed reviews and constructive comments on this manuscript. Editor Don Baker and Associate Editor Julia Semprich are thanked for their efficient handling.

References

Arai, S. (1992) Chemistry of chromian spinel in volcanic rocks as a potential guide to magma chemistry. Mineralogical Magazine, 56(383), 173-184.

Barnes, S.-J., Makovicky, E., Makovicky, M., Rose-Hansen, J., and Karup-Moller, S. (1997) Partition coefficients for Ni, Cu, Pd, Pt, Rh, and Ir between monosulfide solid solution and sulfide liquid and the formation of compositionally zoned Ni – Cu sulfide bodies by fractional crystallization of sulfide liquid. Canadian Journal of Earth Sciences, 34(4), 366-374.

Barnes, S.J. (1986) The effect of trapped liquid crystallization on cumulus mineral compositions in layered intrusions. Contributions to Mineralogy and Petrology, 93(4), 524-531.

Barnes, S.J., Godel, B., Gürer, D., Brenan, J.M., Robertson, J., and Paterson, D. (2013) Sulfide-Olivine Fe-Ni Exchange and the Origin of Anomalously Ni Rich Magmatic Sulfides. Economic Geology, 108(8), 1971-1982.

Barnes, S.J., and Kunilov, V.Y. (2000) Spinels and Mg Ilmenites from the Noril'sk 1 and Talnakh Intrusions and Other Mafic Rocks of the Siberian Flood Basalt Province. Economic Geology, 95(8), 1701-1717.

Barnes, S.J., Mungall, J.E., Le Vaillant, M., Godel, B., Lesher, C.M., Holwell, D., Lightfoot, P.C., Krivolutskaya, N., and Wei, B. (2017) Sulfide-silicate textures in magmatic Ni-Cu-PGE sulfide ore deposits: Disseminated and net-textured ores. American Mineralogist, 102(3), 473-506.

Barnes, S.J., Osborne, G.A., Cook, D., Barnes, L., Maier, W.D., and Godel, B. (2011) The Santa Rita Nickel Sulfide Deposit in the Fazenda Mirabela Intrusion, Bahia, Brazil: Geology, Sulfide Geochemistry, and Genesis. Economic Geology, 106(7), 1083-1110.

Barnes, S.J., and Roeder, P.L. (2001) The range of spinel compositions in terrestrial mafic and ultramafic rocks. Journal of Petrology, 42(12), 2279-2302.

Barnes, S.J., and Tang, Z.-L. (1999) Chrome spinels from the Jinchuan Ni-Cu sulfide deposit, Gansu Province, People's Republic of China. Economic Geology, 94(3), 343-356.

Barnes, S.J., Yao, Z.-S., Mao, Y.J., Jesus, A.P., Yang, S.H., Taranovic, V., and Maier, W.D.

(2022) Nickel in olivine as an exploration indicator for magmatic Ni-Cu sulfide deposits: a data review and re-evaluation. American Mineralogist, doi:10.2138/am-2022-8327.

BGMRXUAR, B.o.G.a.m.R.o.X.U.A.R. (1993) Regional Geology of Xinjiang Uygur Autonomous Region. 1-841 p. Geological Publishing House, Beijing.

Boutroy, E., Dare, S.A.S., Beaudoin, G., Barnes, S.-J., and Lightfoot, P.C. (2014) Magnetite composition in Ni-Cu-PGE deposits worldwide: application to mineral exploration. Journal of Geochemical Exploration, 145, 64-81.

Bowen, N. (1928) The Evolution of the Igneous Rocks, Princeton, Univ. Press, Princeton, New Jersey.

Brenan, J.M. (2003) Effects of fO2, fS2, temperature, and melt composition on Fe-Ni exchange between olivine and sulfide liquid: implications for natural olivine–sulfide assemblages. Geochimica Et Cosmochimica Acta, 67(14), 2663-2681.

Briggs, S.M., Yin, A., Manning, C.E., Chen, Z.-L., Wang, X.-F., and Grove, M. (2007) Late Paleozoic tectonic history of the Ertix Fault in the Chinese Altai and its implications for the development of the Central Asian Orogenic System. Geological Society of America Bulletin, 119(7-8), 944-960.

Cashman, K.V., and Marsh, B.D. (1988) Crystal size distribution (CSD) in rocks and the kinetics and dynamics of crystallization II: Makaopuhi lava lake. Contributions to Mineralogy and Petrology, 99(3), 292-305.

Cookenboo, H., Bustin, R., and Wilks, K. (1997) Detrital chromian spinel compositions used to reconstruct the tectonic setting of provenance; implications for orogeny in the Canadian Cordillera. Journal of Sedimentary Research, 67(1), 116-123.

Czamanske, G.K., Kunilov, V.E., Zientek, M.L., Cabri, L.J., Likhachev, A.P., Calk, L.C., and Oscarson, R.L. (1992) A proton microprobe study of magmatic sulfide ores from the Noril'sk-Talnakh District, Siberia. The Canadian Mineralogist, 30(2), 249-287.

Dare, S.A.S., Barnes, S.-J., Beaudoin, G., Méric, J., Boutroy, E., and Potvin-Doucet, C. (2014) Trace elements in magnetite as petrogenetic indicators. Mineralium Deposita, 49(7), 785-796.

Dare, S.A.S., Barnes, S.J., and Beaudoin, G. (2012) Variation in trace element content of magnetite crystallized from a fractionating sulfide liquid, Sudbury, Canada: Implications for provenance discrimination. Geochimica Et Cosmochimica Acta, 88, 27-50.

Dick, H.B., and Bullen, T. (1984) Chromian spinel as a petrogenetic indicator in abyssal and alpine-type peridotites and spatially associated lavas. Contributions to Mineralogy and Petrology, 86(1), 54-76.

Dowling, S.E., Barnes, S.J., Hill, R.E.T., and Hicks, J.D. (2004) Komatiites and nickel sulfide ores of the Black Swan area, Yilgarn Craton, Western Australia. 2: Geology and genesis of the orebodies. Mineralium Deposita, 39(7), 707-728.

Duan, J., Qian, Z.Z., Feng, Y.Q., Li, C., Ripley, E.M., Xu, G., and Jiao, J.G. (2017) Compositional variations of several Early Permian magmatic sulfide deposits in the Kalatongke district, southern Altai, western China: With genetic and exploration implications. Ore Geology Reviews, 90, 576-590.

Duran, C.J., Barnes, S.-J., Mansur, E.T., Dare, S.A.S., Bédard, L.P., and Sluzhenikin, S.F. (2020) Magnetite Chemistry by LA-ICP-MS Records Sulfide Fractional Crystallization in Massive Nickel-Copper-Platinum Group Element Ores from the Norilsk-Talnakh Mining District (Siberia, Russia): Implications for Trace Element Partitioning into Magnetite. Economic Geology, 115(6), 1245-1266.

Evans, D.M. (2017) Chromite compositions in nickel sulphide mineralized intrusions of the Kabanga-Musongati-Kapalagulu Alignment, East Africa: Petrologic and exploration significance. Ore Geology Reviews, 90, 307-321.

Fleet, M.E., and MacRae, N.D. (1988) Partition of Ni between olivine and sulfide: equilibria with sulfide-oxide liquids. Contributions to Mineralogy and Petrology, 100(4), 462-469.

Fonseca, R.O.C., Campbell, I.H., O'Neill, H.S.C., and Fitzgerald, J.D. (2008) Oxygen solubility and speciation in sulphide-rich mattes. Geochimica et Cosmochimica Acta, 72(11), 2619-2635.

Frost, K.M., and Groves, D.I. (1989) Magmatic contacts between immiscible sulfide and komatiite melts; implications for genesis of Kambalda sulfide ores. Economic Geology, 84(6), 1697-1704.

Gao, J.-F., and Zhou, M.-F. (2013) Magma mixing in the genesis of the Kalatongke dioritic intrusion: Implications for the tectonic switch from subduction to post-collision, Chinese Altay, NW China. Lithos, 162, 236-250.

Gao, J.-F., Zhou, M.-F., Lightfoot, P.C., Wang, C.Y., and Qi, L. (2012) Origin of PGE-Poor and Cu-Rich Magmatic Sulfides from the Kalatongke Deposit, Xinjiang, Northwest China. Economic Geology, 107(3), 481-506.

Gao, J.-F., Zhou, M.-F., Lightfoot, P.C., Wang, C.Y., Qi, L., and Sun, M. (2013) Sulfide Saturation and Magma Emplacement in the Formation of the Permian Huangshandong Ni-Cu Sulfide Deposit, Xinjiang, Northwestern China. Economic Geology, 108(8), 1833-1848.

Giuliani, L., Iezzi, G., Vetere, F., Behrens, H., Mollo, S., Cauti, F., Ventura, G., and Scarlato, P. (2020) Evolution of textures, crystal size distributions and growth rates of plagioclase, clinopyroxene and spinel crystallized at variable cooling rates from a mid-ocean ridge basaltic melt. Earth-Science Reviews, 204, 103165.

Godel, B., Barnes, S.J., Gürer, D., Austin, P., and Fiorentini, M.L. (2013a) Chromite in komatiites: 3D morphologies with implications for crystallization mechanisms. Contributions to Mineralogy and Petrology, 165(1), 173-189.

Godel, B.M., Barnes, S.J., and Barnes, S.-J. (2013b) Deposition Mechanisms of Magmatic Sulphide Liquids: Evidence from High-Resolution X-Ray Computed Tomography and Trace Element Chemistry of Komatiite-hosted Disseminated Sulphides. Journal of Petrology.

Higgins, M.D. (2002) Closure in crystal size distributions (CSD), verification of CSD calculations, and the significance of CSD fans. American Mineralogist, 87(1), 171-175.

Higgins, M.D. (2006) Quantitative textural measurements in igneous and metamorphic petrology. Cambridge University Press.

Hill, R., and Roeder, P. (1974) The Crystallization of Spinel from Basaltic Liquid as a Function of Oxygen Fugacity. The Journal of Geology, 82(6), 709-729.

Irvine, T.N. (1965) CHROMIAN SPINEL AS A PETROGENETIC INDICATOR: PART 1. THEORY. Canadian Journal of Earth Sciences, 2(6), 648-672.

-. (1967) CHROMIAN SPINEL AS A PETROGENETIC INDICATOR: PART 2. PETROLOGIC APPLICATIONS. Canadian Journal of Earth Sciences, 4(1), 71-103.

J. Wood, B., and Virgo, D. (1989) Upper mantle oxidation state: Ferric iron contents of Iherzolite spinels by 57Fe Mössbauer spectroscopy and resultant oxygen fugacities. Geochimica et Cosmochimica Acta, 53(6), 1277-1291.

Jackson, E. (1969) Chemical variation in coexisting chromite and olivine in chromitite zones of the Stillwater Complex, Montana. In Magmatic Ore Deposits. Econ. Geol. Monogr., 4, 41-71.

Jiao, J., Han, F., Zhao, L., Duan, J., and Wang, M. (2019) Magnetite Geochemistry of the Jinchuan Ni-Cu-PGE Deposit, NW China: Implication for Its Ore-Forming Processes. Minerals, 9(10), 593.

Kang, Z., Qin, K.-Z., Mao, Y.-J., Tang, D.-M., and Yao, Z.-S. (2020) The formation of a magmatic CuNi sulfide deposit in mafic intrusions at the Kalatongke, NW China: Insights from amphibole mineralogy and composition. Lithos, 352-353, 105317.

Lehmann, J. (1983) Diffusion between olivine and spinel: application to geothermometry. Earth and Planetary Science Letters, 64(1), 123-138.

Li, C., Zhang, M.J., Fu, P., Qian, Z.Z., Hu, P.Q., and Ripley, E.M. (2012) The Kalatongke magmatic Ni-Cu deposits in the Central Asian Orogenic Belt, NW China: product of slab window magmatism? Mineralium Deposita, 47(1-2), 51-67.

Liu, Y., Hu, Z., Gao, S., Günther, D., Xu, J., Gao, C., and Chen, H. (2008) In situ analysis of major and trace elements of anhydrous minerals by LA-ICP-MS without applying an internal standard. Chemical Geology, 257(1), 34-43.

Lu, Y., Lesher, C.M., and Deng, J. (2019) Geochemistry and genesis of magmatic Ni-Cu-(PGE) and PGE-(Cu)-(Ni) deposits in China. Ore Geology Reviews, 107, 863-887.

Mao, J.W., Pirajno, F., Zhang, Z.H., Chai, F.M., Wu, H., Chen, S.P., Cheng, L.S., Yang, J.M., and Zhang, C.Q. (2008) A review of the Cu-Ni sulphide deposits in the Chinese Tianshan and Altay orogens (Xinjiang Autonomous Region, NW China): Principal characteristics and ore-forming processes. Journal of Asian Earth Sciences, 32(2-4), 184-203.

Mao, Y.-J., Barnes, S.J., Godel, B., Schoneveld, L., Qin, K.-Z., Tang, D., Williams, M., and Kang, Z. (2022a) Sulfide Ore Formation of the Kalatongke Ni-Cu Deposit as Illustrated by Sulfide Textures. Economic Geology, doi:10.5382/econgeo.4914.

Mao, Y.-J., Qin, K.-Z., Barnes, S.J., Ferraina, C., Iacono-Marziano, G., Verrall, M., Tang, D., and Xue, S. (2018) A revised oxygen barometry in sulfide-saturated magmas and application to the Permian magmatic Ni–Cu deposits in the southern Central Asian Orogenic Belt. Mineralium Deposita, 53(6), 731-755.

Mao, Y.-J., Qin, K.-Z., Li, C., and Tang, D.-M. (2015) A modified genetic model for the Huangshandong magmatic sulfide deposit in the Central Asian Orogenic Belt, Xinjiang, western China. Mineralium Deposita, 50(1), 65-82.

Mao, Y.-J., Qin, K.-Z., Li, C., Xue, S.C., and Ripley, E.M. (2014) Petrogenesis and ore genesis of the Permian Huangshanxi sulfide ore-bearing mafic-ultramafic intrusion in the Central Asian Orogenic Belt, western China. Lithos, 200(0), 111-125.

Mao, Y.-J., Schoneveld, L., Barnes, S.J., Williams, M.J., Su, B.-X., Ruprecht, P., Evans, N.J., and Qin, K.-Z. (2022b) Coupled Li-P Zoning and Trace Elements of Olivine from Magmatic Ni-Cu Deposits: Implications for Postcumulus Re-Equilibration in Olivine. Journal of Petrology, 63(3), 1-22.

Marsh, B.D. (1988) Crystal size distribution (CSD) in rocks and the kinetics and dynamics of crystallization. Contributions to Mineralogy and Petrology, 99(3), 277-291.

Maurel, C., and Maurel, P. (1982) Etude expérimentale de la solubilité du chrome dans les bains silicatés basiques et sa distribution entre liquide et minéraux coexistants: conditions d'existence du spinelle chromifére. Bull Minéral, 105, 197-202.

Moilanen, M., Hanski, E., Konnunaho, J., Törmänen, T., Yang, S.H., Lahaye, Y., O'Brien, H., and Illikainen, J. (2020) Composition of iron oxides in Archean and Paleoproterozoic mafic-ultramafic hosted Ni-Cu-PGE deposits in northern Fennoscandia: application to mineral exploration. Mineralium Deposita, 55(8), 1515-1534.

Naldrett, A.J. (1969) A Portion of System Fe-S-O between 900 and 1080 Degrees C and Its Application to Sulfide Ore Magmas. Journal of Petrology, 10(2), 171-201.

Naldrett, A.J., Singh, J., Krstic, S., and Li, C. (2000) The Mineralogy of the Voisey's Bay Ni-Cu-Co Deposit, Northern Labrador, Canada: Influence of Oxidation State on

Textures and Mineral Compositions. Economic Geology, 95(4), 889-900.

O'Neill, H.S.C., and Wall, V.J. (1987) The Olivine—Orthopyroxene—Spinel Oxygen Geobarometer, the Nickel Precipitation Curve, and the Oxygen Fugacity of the Earth's Upper Mantle. Journal of Petrology, 28(6), 1169-1191.

Qian, Z.Z., Wang, J.Z., Jiang, C.Y., Jiao, J.G., Yan, H.Q., He, K., and Sun, T. (2009) Geochemistry characters of platinum-group elements and its significances on the process of mineralization in the Kalatongke Cu-Ni sulfide deposit, Xinjiang, China. Acta Petrologica Sinica, 25(4), 832-844.

Qin, K.-Z., Su, B.-X., Sakyi, P.A., Tang, D.M., Li, X.H., Sun, H., Xiao, Q.H., and Liu, P.P. (2011) Sims zircon U-Pb geochronology and Sr-Nd isotopes of Ni-Cu-bearing mafic-ultramafic intrusions in Eastern tianshan and Beishan in correlation with flood basalts in Tarim basin (NW china): Constraints on a Ca. 280 Ma mantle plume. American Journal of Science, 311(3), 237-260.

Roeder, P.L. (1994) Chromite; from the fiery rain of chondrules to the Kilauea Iki lava lake. The Canadian Mineralogist, 32(4), 729-746.

Roeder, P.L., and Campbell, I.H. (1985) The effect of postcumulus reactions on compositions of chrome-spinels from the Jimberlana Intrusion. Journal of Petrology, 26, 763-786.

Rudnick, R., and Gao, S. (2003) Composition of the continental crust. Treatise on geochemistry, 3, 1-64.

Sack, R.O., and Ghiorso, M.S. (1991) Chromian spinels as petrogenetic indicators: Thermodynamics and petrological applications. American Mineralogist, 76(5-6), 827-847.

Schoneveld, L., Barnes, S.J., Williams, M., Le Vaillant, M., and Paterson, D. (2020) Silicate and Oxide Mineral Chemistry and Textures of the Norilsk-Talnakh Ni-Cu-Platinum Group Element Ore-Bearing Intrusions. Economic Geology, 115(6), 1227-1243.

Sengör, A., Natal'In, B., and Burtman, V. (1993) Evolution of the Altaid tectonic collage and Palaeozoic crustal growth in Eurasia. Nature, 364, 299-307.

Song, X.-Y., Wang, K.-Y., Barnes, S.J., Yi, J.-N., Chen, L.-M., and Schoneveld, L.E. (2020) Petrogenetic insights from chromite in ultramafic cumulates of the Xiarihamu intrusion, northern Tibet Plateau, China. American Mineralogist, 105(4), 479-497.

Song, X.Y., and Li, X.R. (2009) Geochemistry of the Kalatongke Ni-Cu-(PGE) sulfide deposit, NW China: implications for the formation of magmatic sulfide mineralization in a postcollisional environment. Mineralium Deposita, 44(3), 303-327.

Taranovic, V., Barnes, S.J., Beresford, S., Williams, M., MacRae, C., and Schoneveld, L.E. (2021) Nova-Bollinger Ni-Cu Sulfide Ore Deposits, Fraser Zone, Western Australia: Petrogenesis of the Host Intrusions. Economic Geology, In press.

Wang, R., and Zhao, C. (1991) Intruson 1 of the Kalatongke magmatic Ni-Cu deposit, Xinjiang. Geological publication, Beijing.

Ward, L.A., Holwell, D.A., Barry, T.L., Blanks, D.E., and Graham, S.D. (2018) The use of magnetite as a geochemical indicator in the exploration for magmatic Ni-Cu-PGE sulfide deposits: A case study from Munali, Zambia. Journal of Geochemical Exploration, 188, 172-184.

Wei, B., Yan Wang, C., Lahaye, Y., Xie, L., and Cao, Y. (2019) S and C Isotope Constraints for Mantle-Derived Sulfur Source and Organic Carbon-Induced Sulfide Saturation of Magmatic Ni-Cu Sulfide Deposits in the Central Asian Orogenic Belt, North China. Economic Geology, 114(4), 787-806.

Williams, M.J., Schoneveld, L., Mao, Y., Klump, J., Gosses, J., Dalton, H., Bath, A., and Barnes, S. (2020) pyrolite: Python for geochemistry. Journal of Open Source Software, 5(50), 2314.

Xiao, W.J., Han, C.M., Yuan, C., Sun, M., Lin, S.F., Chen, H.L., Li, Z.L., Li, J.L., and Sun, S. (2008) Middle Cambrian to Permian subduction-related accretionary orogenesis of Northern Xinjiang, NW China: Implications for the tectonic evolution of central Asia. Journal of Asian Earth Sciences, 32(2-4), 102-117.

Xue, S., Qin, K., Li, C., Tang, D., Mao, Y., Qi, L., and Ripley, E.M. (2016) Geochronological, Petrological, and Geochemical Constraints on Ni-Cu Sulfide Mineralization in the Poyi Ultramafic-Troctolitic Intrusion in the Northeast Rim of the Tarim Craton, Western China. Economic Geology, 111(6), 1465-1484.

Zhang, Z.C., Mao, J.W., Chai, F.M., Yan, S.H., Chen, B.L., and Pirajno, F. (2009) Geochemistry of the Permian Kalatongke Mafic Intrusions, Northern Xinjiang, Northwest China: Implications for the Genesis of Magmatic Ni-Cu Sulfide Deposits. Economic Geology, 104(2), 185-203.

Figure captions

Fig.1 Simplified geological map of the East Junggar terrane (after Song and Li, 2009) and the Central Asian Orogenic Belt (inset) (after Sengör et al., 1993), showing the location of the Kalatongke Ni-Cu deposit. The small yellow circles in the inset show the location of other Ni-Cu deposits in the Central Asian Orogenic Belt.

Fig. 2 Simplified geological map (a) and sections (b-d) of the Kalatongke deposit, showing the distribution of the mafic intrusions and the variable types of sulfide mineralization within them. The geological map is from Wang and Zhao (1991), whereas the sections are from Xinxin Mining Industry Co. Ltd based on the latest exploration data.

Fig.3 Reflected light images (a-d), BSE image (e), and processed images (f-g) show the 2D morphology, grain size, and spatial distributions of Cr-spinel, Cr-magnetite, and magnetite in the disseminated and massive ores. Most Cr-magnetite grains are euhedral-shaped (a, b), whereas some irregular magnetite grains are shown in massive ores (c). Dendritic textured magnetite from a massive ore (d). The grain size of Cr-spinel and Cr-magnetite in silicates is smaller than that of Cr-magnetite included in disseminated sulfides (e, f), which is significantly smaller than that included in massive sulfides (g). Note that Cr-magnetite in the disseminated sulfides tends to occur at the rim of the sulfide pockets (a, b, e). The high-resolution versions of the processed images (f, g) can be downloaded from online Supplementary Material 1 and 2. Abbreviations: Ap-apatite, Cpy-chalcopyrite, Cr-Sp for Cr-spinel included in olivine, Cr-Mt for Cr-magnetite included in other silicates and disseminated sulfide, Hb-hornblende, Mt-magnetite, Ol-olivine, Opx-orthopyroxene, Pl-Plagioclase, Pn-pentlandite, Po-pyrrhotite.

Fig. 4 Crystal size distribution (CSD) of Cr-magnetite grains in silicates, Cr-magnetite crystals in disseminated, and magnetite in massive sulfides. The CSDs illustrate log-linear distributions of variable slopes and intercepts, suggesting crystallization under different conditions. The processed high-resolution image with touched grains separated was used for crystal size distribution analysis (Fig. 3f-g, Supplementary Material 1 and 2).

Fig. 5 Major contents (a-e) and Cr# variation (f) in Cr-spinel, Cr-magnetite, and magnetite of the Kalatongke deposit. Mg# equals 100* Mg/(Mg+Fe), Cr# equals 100* Cr/(Cr+Al). The Al_2O_3 and Cr_2O_3 contents in magnetite are close to the detection limit and not plotted in the Cr# plot (f). The composition of Cr-spinel in olivine and silicate minerals composition from other Ni-Cu deposits in the Central Asian Orogenic belt (CAOB), which includes the Huangshandong, Huangshanxi, Xiangshan, and Huangshannan deposits (from Mao et al., 2014, 2015 and references therein), is plotted for comparison.

Fig.6 Al-Fe-Cr ternary diagram for the Cr-spinel, Cr-magnetite, and magnetite of the Kalatongke deposit, in comparison with that from other regional deposits and the Noril'sk camp. The Kalatongke data are from this study. The Norilsk spinel data are from Schoneveld et al. (2020), the regional deposits and their data source are listed in the caption of Fig. 5. The Cr-Al trend (two-headed gray arrow) and Fe-Ti trend (black arrow) are from Barnes and Roeder (2001).

Fig. 7 Trace element variations of Cr-spinel, Cr-magnetite, and magnetite from the Kalatongke deposit. The Cr-magnetite grains enclosed in disseminated sulfides have similar V, Sc, Ga, Mo, Zr, and Nb concentrations (a-f) but depleted Ni, Co, and Zn (g-i) contents relative to those enclosed in silicates. For the Cr-magnetite in disseminated sulfides, no detectable compositional difference is shown for the Cr-magnetite in pyrrhotite and that in chalcopyrite. For the magnetite in massive sulfides, in contrast, the compositional difference of some trace elements (V, Ni, Co, Zn, a, g, h, i) is shown for the magnetite in pyrrhotite and that in chalcopyrite. See the text for a detailed explanation.

Fig. 8 Correlation between Ni, Co, Zn content and ferrous Fe in the X site of the Cr-spinel, Cr-magnetite, and magnetite from the Kalatongke deposit. The ratio is calculated by ferrous Fe to other elements.

Fig.9 A multi-element diagram for Cr-spinel, Cr-magnetite, and magnetite of the Kalatongke, normalized to bulk continental crust (Rudnick and Gao, 2003). (a) Cr-spinel in olivine and Cr-magnetite in other silicates, (b) Cr-magnetite included in disseminated sulfides, (c) Magnetite in massive ores. Trace elements are ordered according to increasing compatibility into magnetite from left to right (after Dare et al. 2014).

Fig. 10 The discrimination diagrams of the origin of the massive sulfide in terms of the association of Cr versus Ti (a), V (b), and Ni (c) contents in magnetite. The magnetite included in the massive sulfide of the Kalatongke deposit plot on the region of the magnetite crystallized from the evolved Fe-rich sulfide melt. The Cr-spinel in silicates and Cr-magnetite in disseminated sulfides, which have been attributed to equilibrium crystallization, are plotted for comparison. The gray fields show the composition of magnetite that crystallized from massive sulfides with variable fractionation degrees, which was built based on the magnetite from the Sudbury deposit (Dare et al., 2012; Boutroy et al., 2014). The magnetite from the Huangshandong deposit is from Gao et al. (2013).

Figure 1

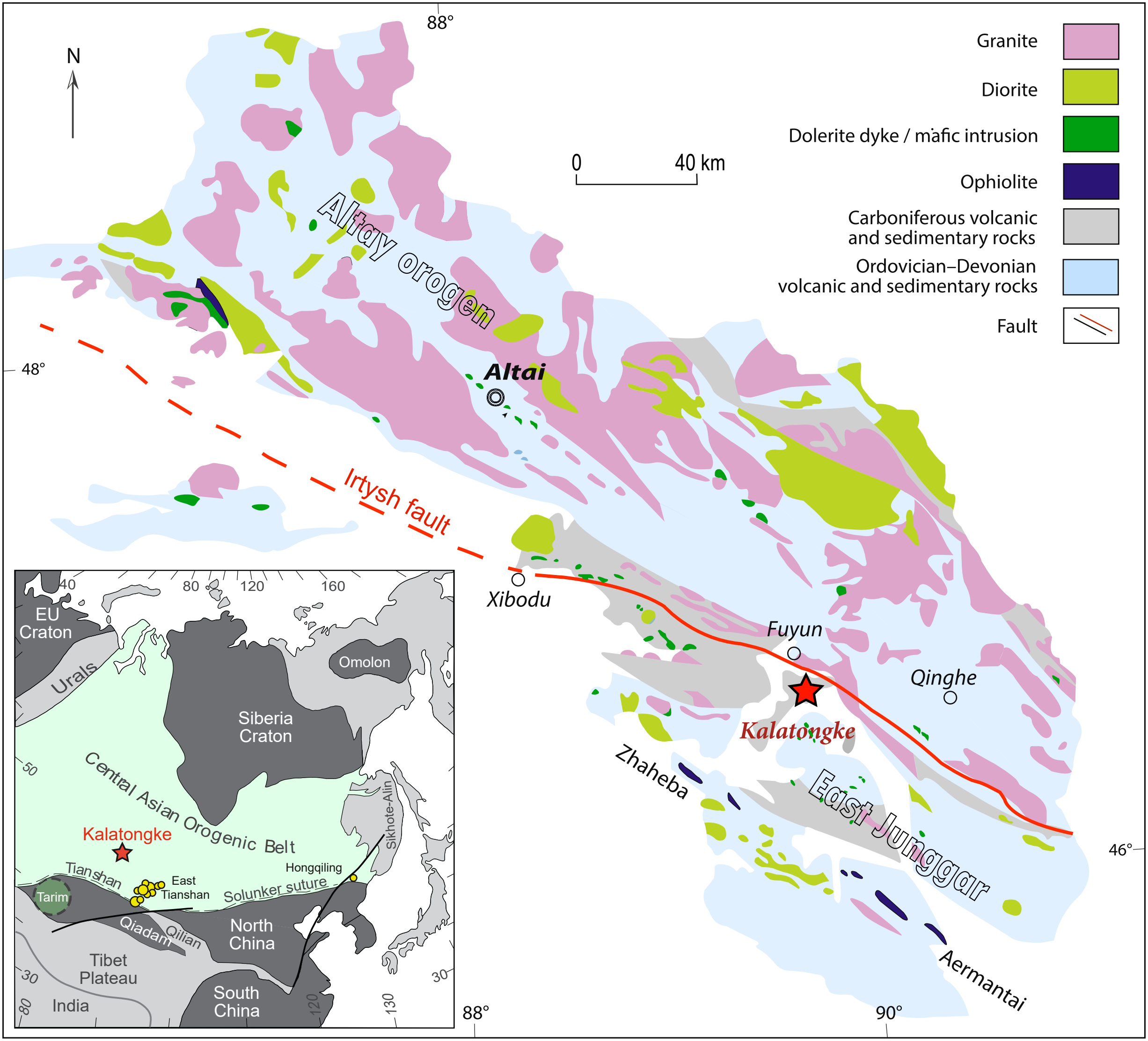

88°
N
Granite
Diorite
Dolerite dyke / mafic intrusion
Ophiolite
Carboniferous volcanic and sedimentary rocks
Ordovician–Devonian volcanic and sedimentary rocks
Fault
0
40 km
Altay orogen
48°
Altai
Irtysh fault
Xibodu
Fuyun
Qinghe
Kalatongke
Zhaheba
East Junggar
Aermantai
46°
88°
90°
40
80
120
160
EU Craton
Urals
Omolon
Siberia Craton
50
Central Asian Orogenic Belt
Kalatongke
Sikhote-Alin
Hongqiling
Tianshan
East Tianshan
Solunker suture
Tarim
Qiadam
Qilian
North China
Tibet Plateau
30
30
India
South China
80
120
130

Figure 2

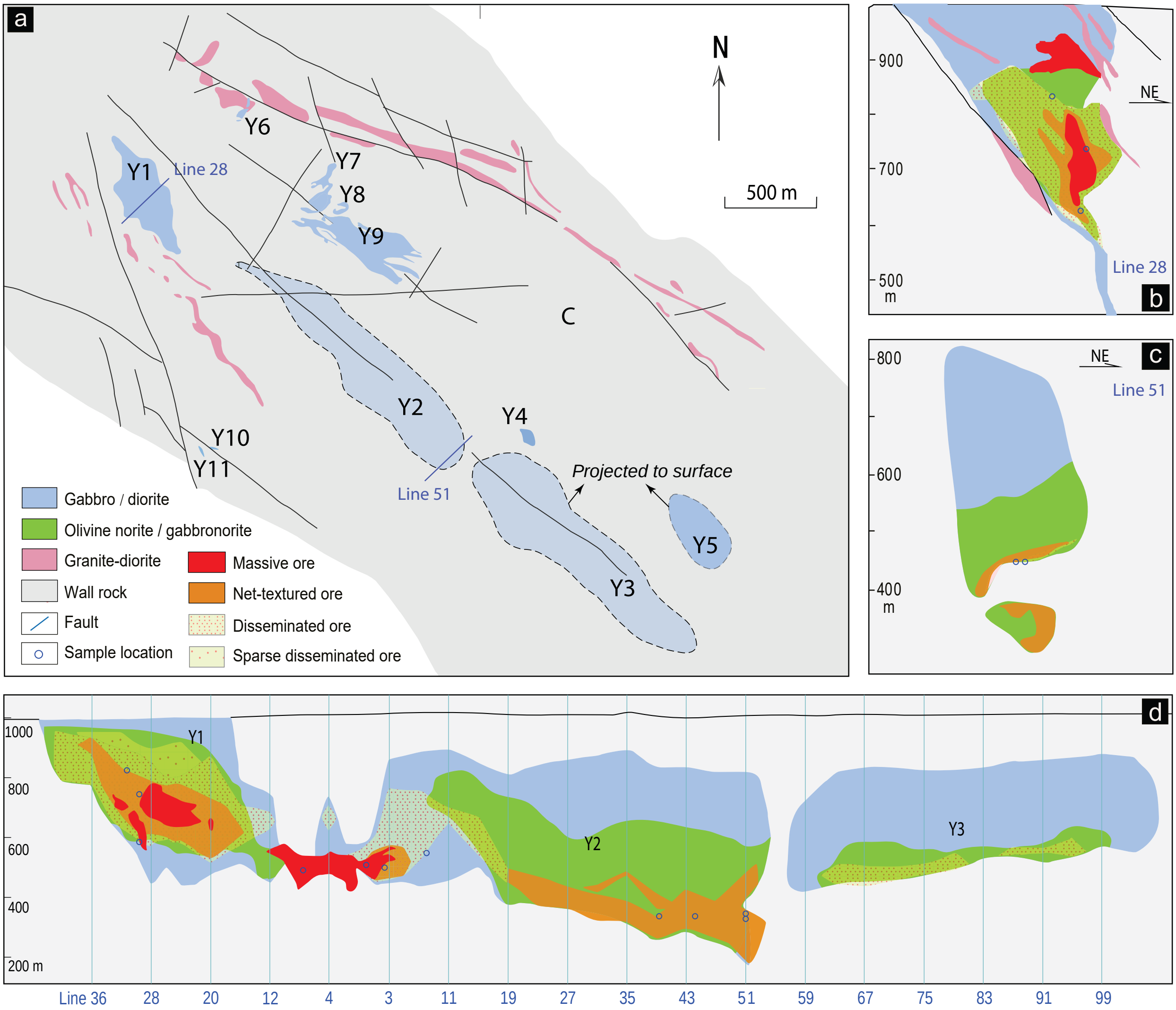
a
N
500 m
Y1
Line 28
Y6
Y7
Y8
Y9
Y2
Y4
Y10
Y11
Line 51
Projected to surface
Y5
Y3
C
Gabbro / diorite
Olivine norite / gabbronorite
Granite-diorite
Wall rock
Fault
Sample location
Massive ore
Net-textured ore
Disseminated ore
Sparse disseminated ore
b
900
700
500 m
NE
Line 28
c
800
600
400 m
NE
Line 51
d
1000
800
600
400
200 m
Y1
Y2
Y3
Line 36
28
20
12
4
3
11
19
27
35
43
51
59
67
75
83
91
99

Figure 3

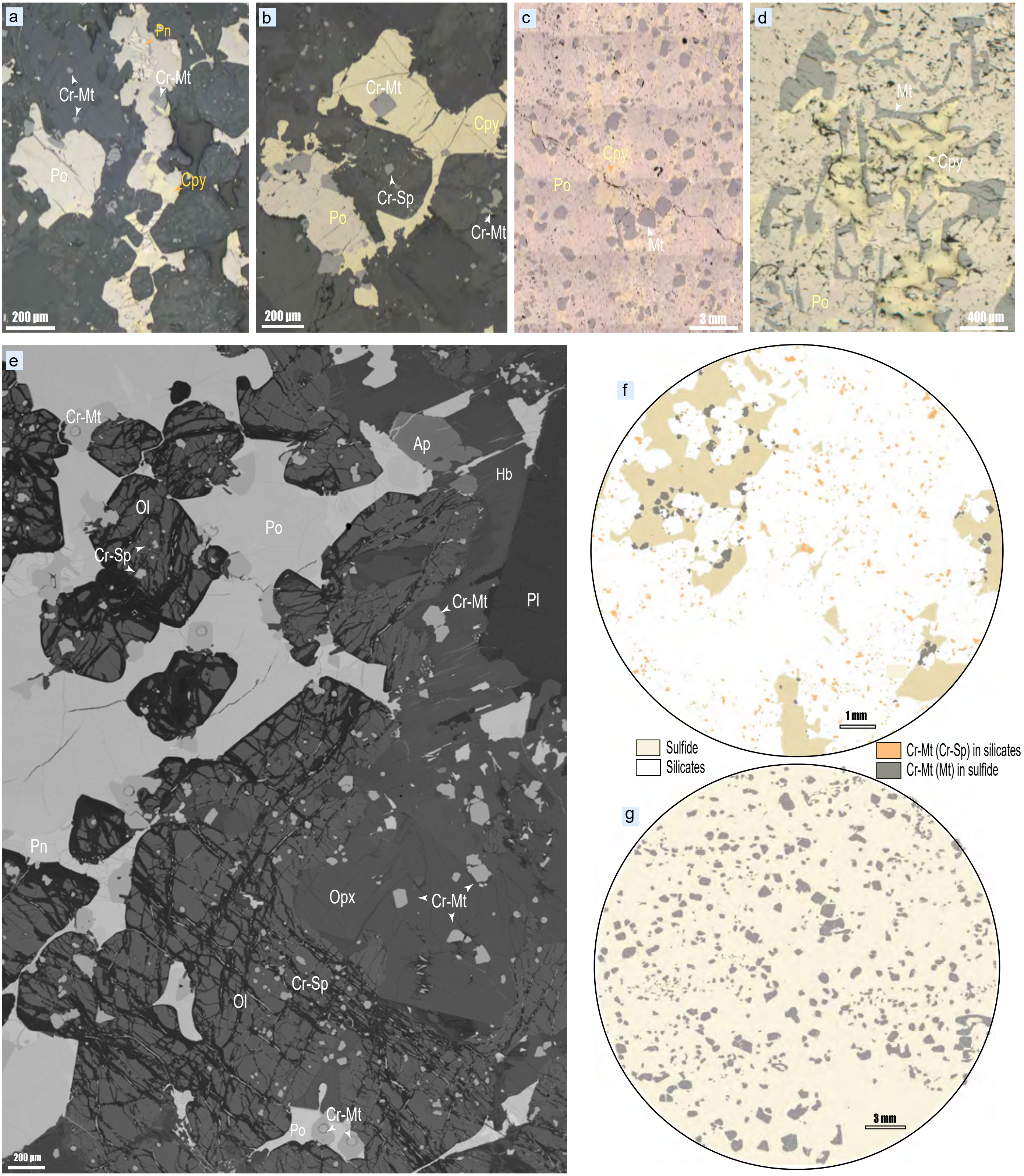
a
Pn
Cr-Mt
Cr-Mt
Po
Cpy
200 μm
b
Cr-Mt
Cpy
Cr-Sp
Po
Cr-Mt
200 μm
c
Cpy
Po
Mt
3 mm
d
Mt
Cpy
Po
400 μm
e
Cr-Mt
Ap
Hb
Ol
Po
Cr-Sp
Cr-Mt
Pl
Pn
Opx
Cr-Mt
Cr-Sp
Ol
Cr-Mt
Po
200 μm
f
1 mm
Sulfide
Silicates
Cr-Mt (Cr-Sp) in silicates
Cr-Mt (Mt) in sulfide
g
3 mm

Figure 4

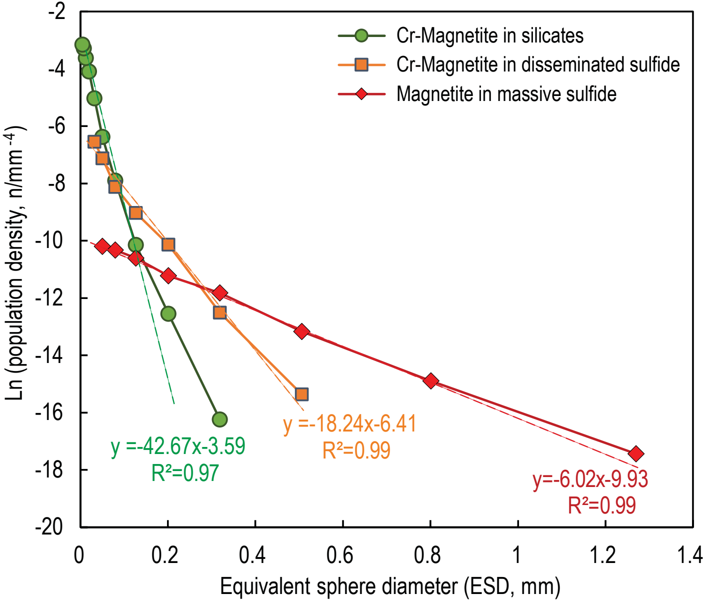
-2
-4
-6
-8
-10
-12
-14
-16
-18
-20
0
0.2
0.4
0.6
0.8
1
1.2
1.4
Ln (population density, n/mm^{-4})
Equivalent sphere diameter (ESD, mm)
Cr-Magnetite in silicates
Cr-Magnetite in disseminated sulfide
Magnetite in massive sulfide
y =-42.67x-3.59
R²=0.97
y =-18.24x-6.41
R²=0.99
y=-6.02x-9.93
R²=0.99

Figure 5

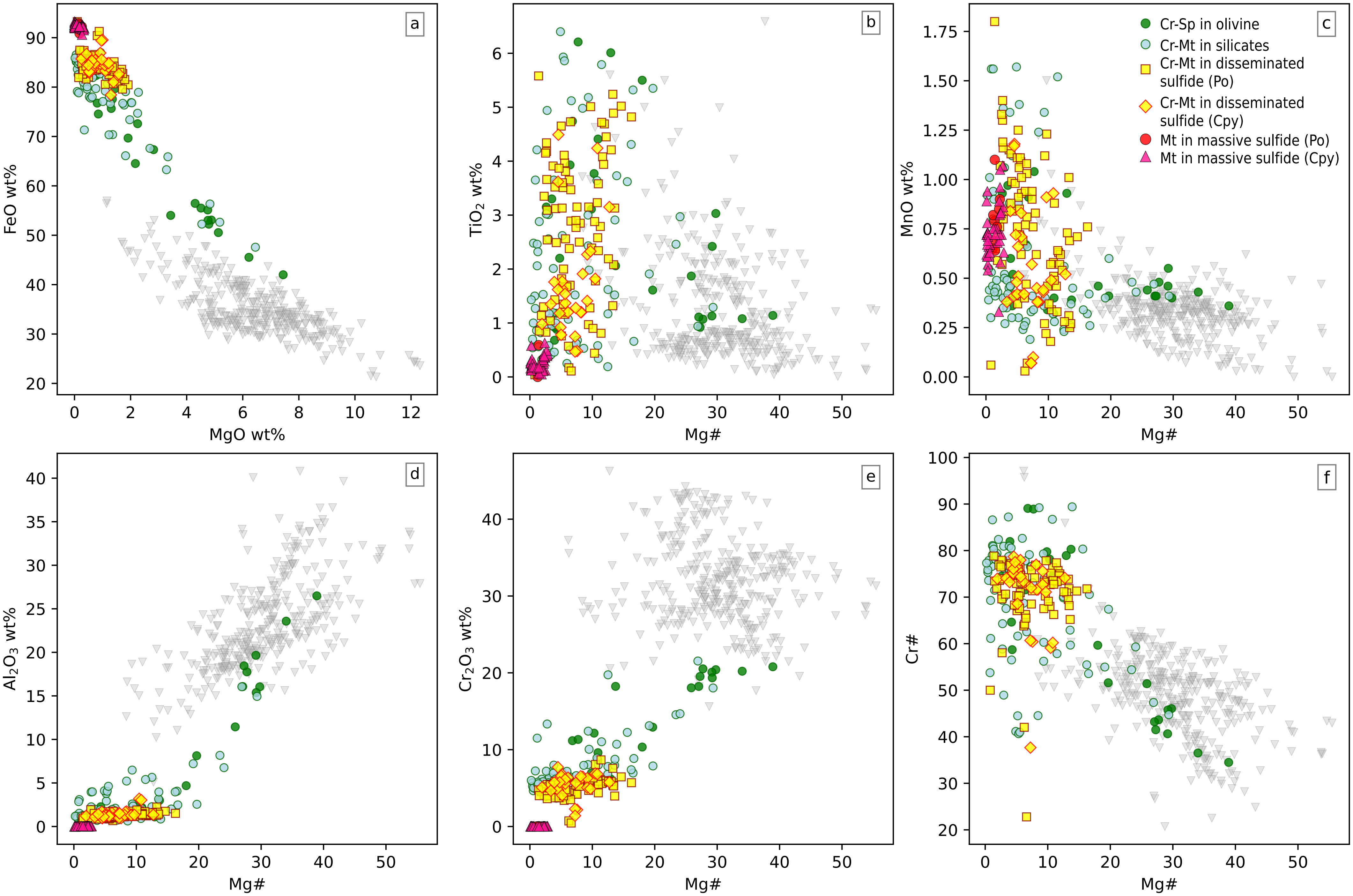
a
FeO wt%
MgO wt%
b
TiO$_2$ wt%
Mg#
c
MnO wt%
Mg#
Cr-Sp in olivine
Cr-Mt in silicates
Cr-Mt in disseminated sulfide (Po)
Cr-Mt in disseminated sulfide (Cpy)
Mt in massive sulfide (Po)
Mt in massive sulfide (Cpy)
d
Al$_2$O$_3$ wt%
Mg#
e
Cr$_2$O$_3$ wt%
Mg#
f
Cr#
Mg#

Figure 6

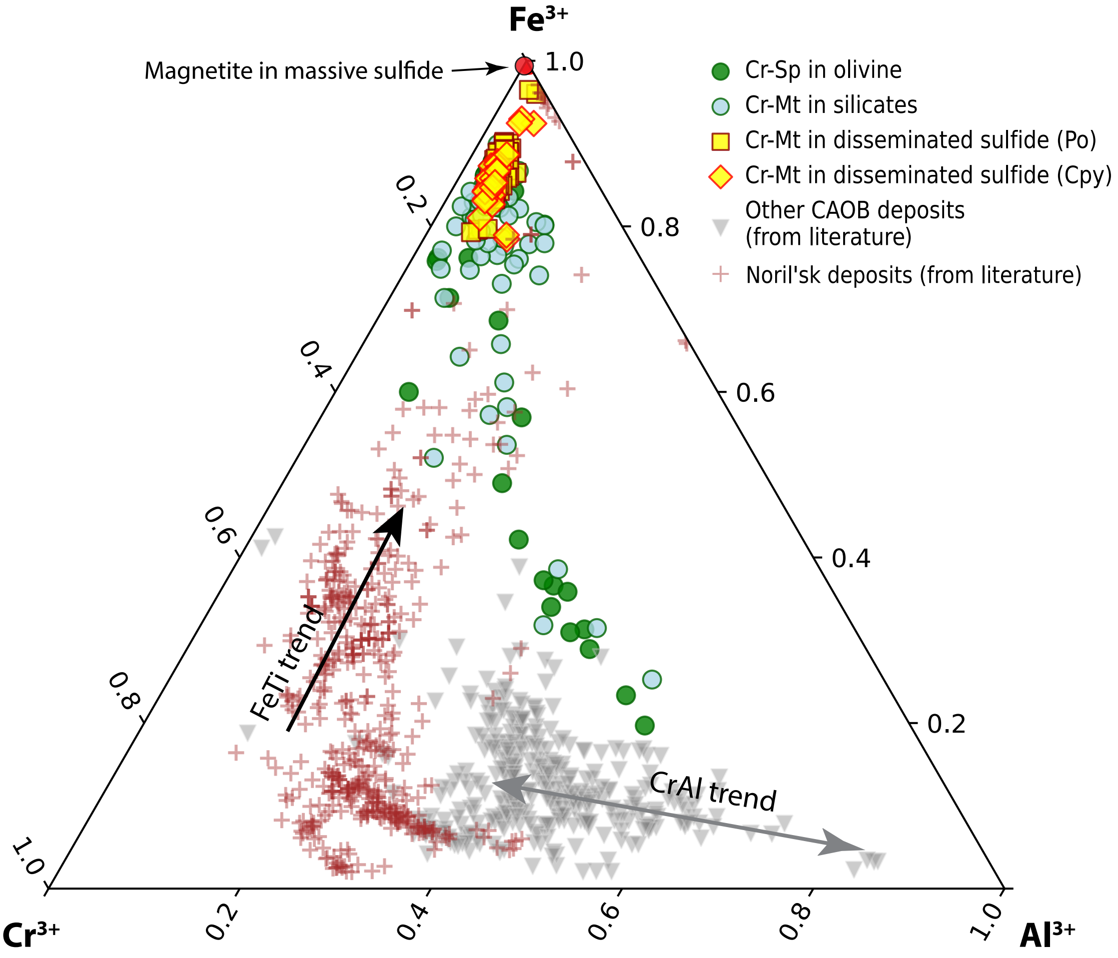
Fe^{3+}
Cr^{3+}
Al^{3+}
Magnetite in massive sulfide
1.0
0.8
0.6
0.4
0.2
FeTi trend
CrAl trend
Cr-Sp in olivine
Cr-Mt in silicates
Cr-Mt in disseminated sulfide (Po)
Cr-Mt in disseminated sulfide (Cpy)
Other CAOB deposits (from literature)
Noril'sk deposits (from literature)

Figure 7

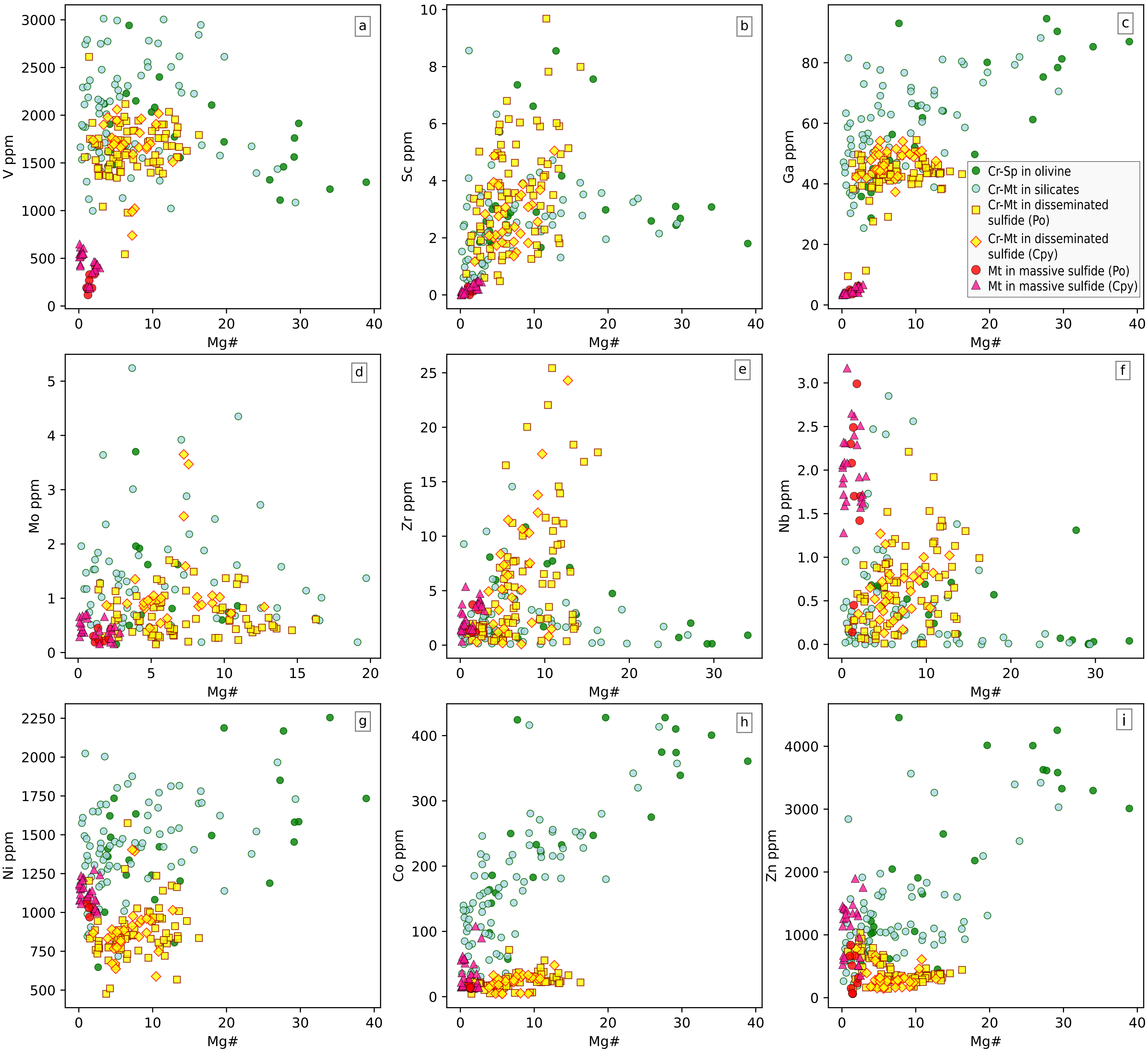
a
V ppm
Mg#
b
Sc ppm
Mg#
c
Ga ppm
Mg#
Cr-Sp in olivine
Cr-Mt in silicates
Cr-Mt in disseminated sulfide (Po)
Cr-Mt in disseminated sulfide (Cpy)
Mt in massive sulfide (Po)
Mt in massive sulfide (Cpy)
d
Mo ppm
Mg#
e
Zr ppm
Mg#
f
Nb ppm
Mg#
g
Ni ppm
Mg#
h
Co ppm
Mg#
i
Zn ppm
Mg#

Figure 8

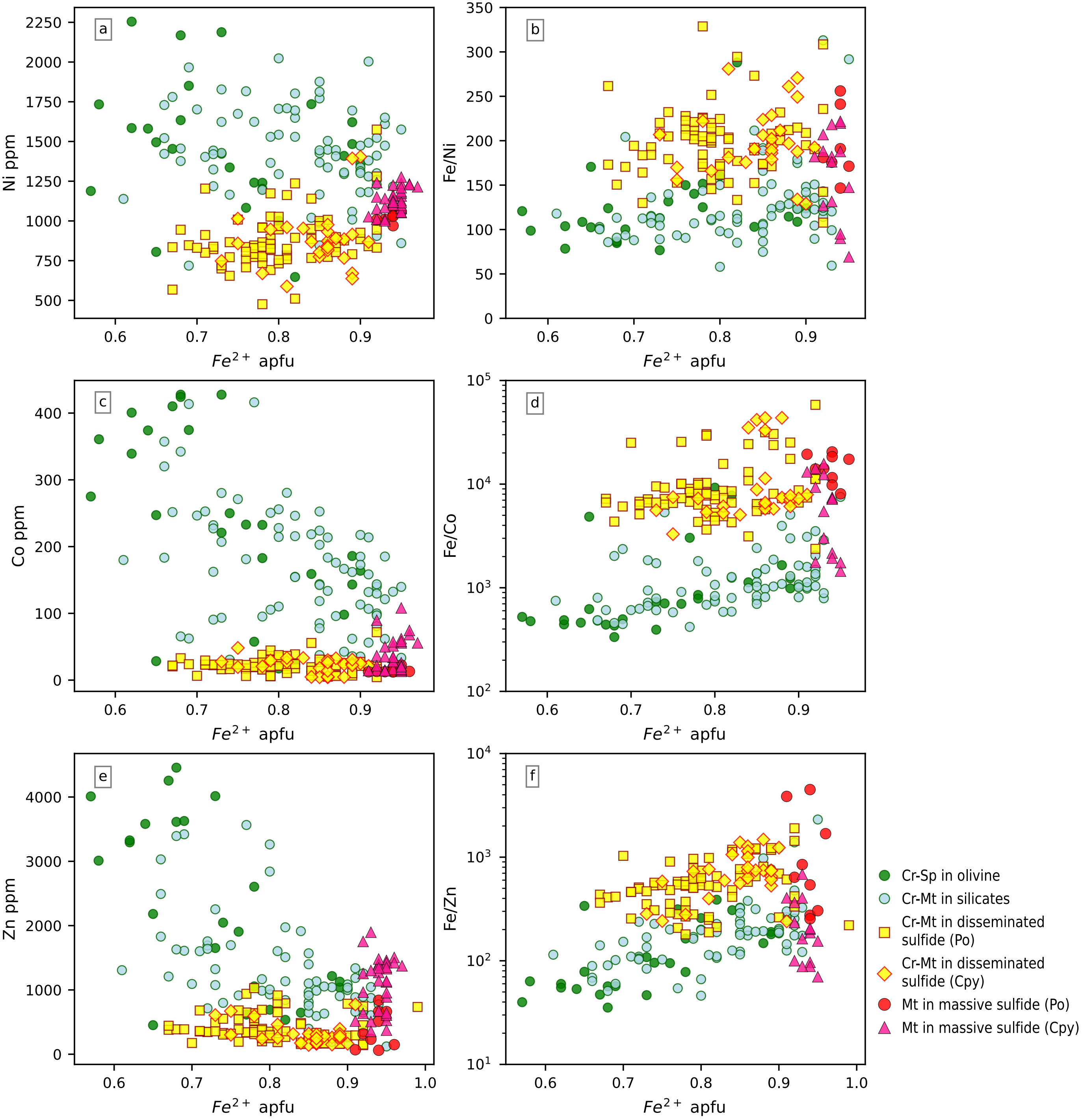
a
Ni ppm
2250
2000
1750
1500
1250
1000
750
500
0.6
0.7
0.8
0.9
Fe^{2+} apfu
b
Fe/Ni
350
300
250
200
150
100
50
0
Fe^{2+} apfu
c
Co ppm
400
300
200
100
0
Fe^{2+} apfu
d
Fe/Co
10^5
10^4
10^3
10^2
Fe^{2+} apfu
e
Zn ppm
4000
3000
2000
1000
0
1.0
Fe^{2+} apfu
f
Fe/Zn
10^4
10^3
10^2
10^1
Fe^{2+} apfu
Cr-Sp in olivine
Cr-Mt in silicates
Cr-Mt in disseminated sulfide (Po)
Cr-Mt in disseminated sulfide (Cpy)
Mt in massive sulfide (Po)
Mt in massive sulfide (Cpy)

Figure 9

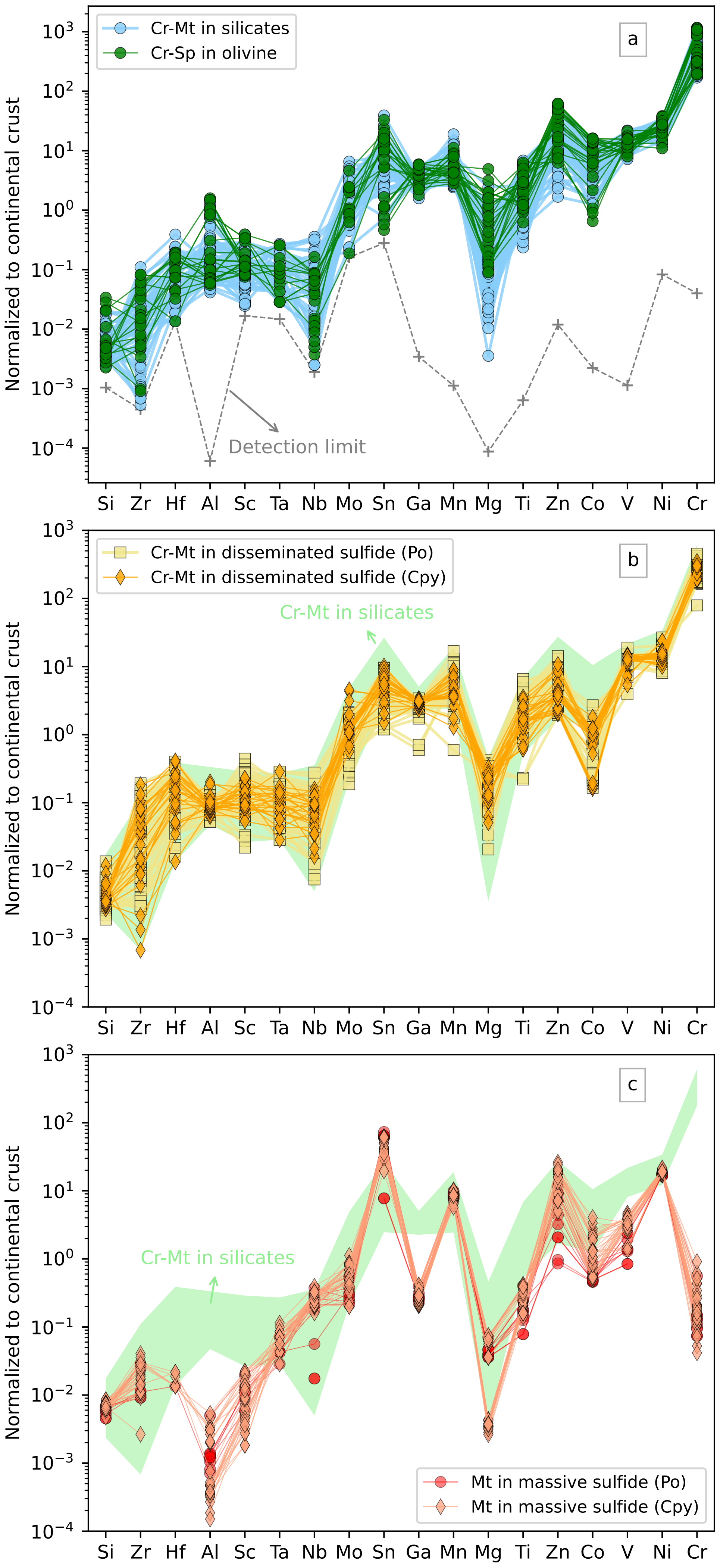
a
Cr-Mt in silicates
Cr-Sp in olivine
Detection limit
Normalized to continental crust
10^{-4} 10^{-3} 10^{-2} 10^{-1} 10^{0} 10^{1} 10^{2} 10^{3}
Si Zr Hf Al Sc Ta Nb Mo Sn Ga Mn Mg Ti Zn Co V Ni Cr
b
Cr-Mt in disseminated sulfide (Po)
Cr-Mt in disseminated sulfide (Cpy)
Cr-Mt in silicates
Normalized to continental crust
Si Zr Hf Al Sc Ta Nb Mo Sn Ga Mn Mg Ti Zn Co V Ni Cr
c
Cr-Mt in silicates
Mt in massive sulfide (Po)
Mt in massive sulfide (Cpy)
Normalized to continental crust
Si Zr Hf Al Sc Ta Nb Mo Sn Ga Mn Mg Ti Zn Co V Ni Cr

Figure 10

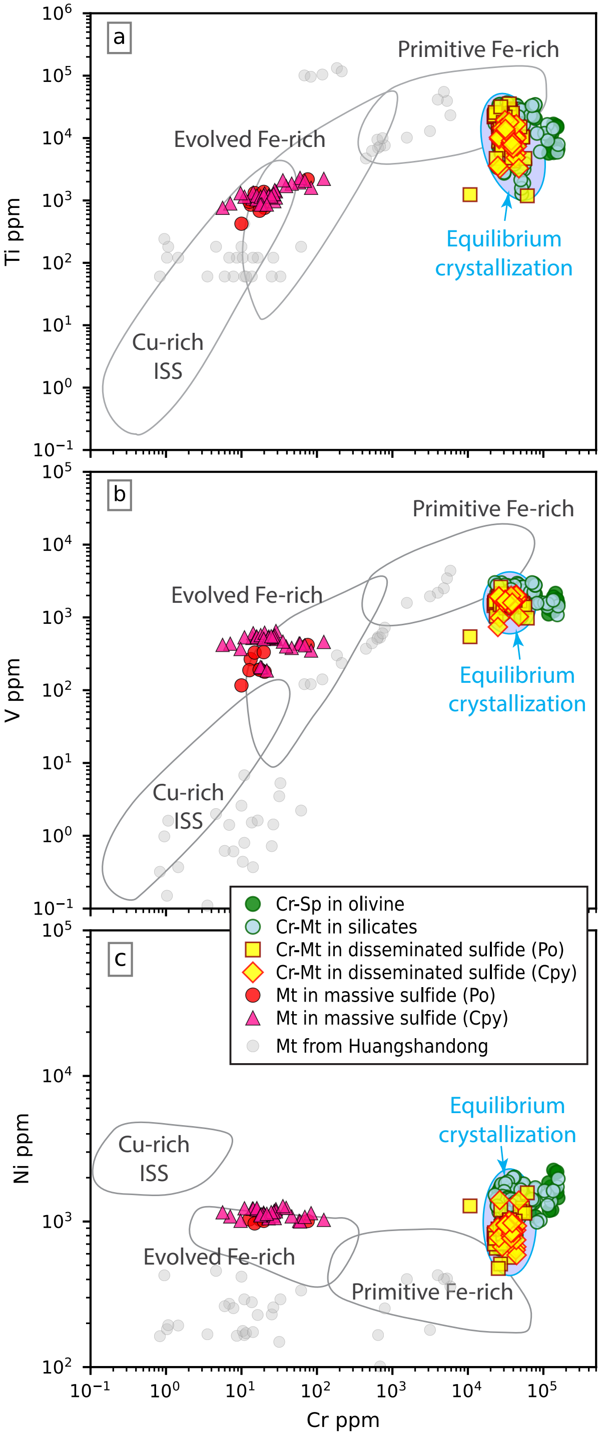
a
Primitive Fe-rich
Evolved Fe-rich
Cu-rich ISS
Equilibrium crystallization
Ti ppm
10⁻¹ 10⁰ 10¹ 10² 10³ 10⁴ 10⁵ 10⁶
b
Primitive Fe-rich
Evolved Fe-rich
Cu-rich ISS
Equilibrium crystallization
V ppm
10⁻¹ 10⁰ 10¹ 10² 10³ 10⁴ 10⁵
c
Cu-rich ISS
Evolved Fe-rich
Primitive Fe-rich
Equilibrium crystallization
Ni ppm
10² 10³ 10⁴ 10⁵
Cr-Sp in olivine
Cr-Mt in silicates
Cr-Mt in disseminated sulfide (Po)
Cr-Mt in disseminated sulfide (Cpy)
Mt in massive sulfide (Po)
Mt in massive sulfide (Cpy)
Mt from Huangshandong
10⁻¹ 10⁰ 10¹ 10² 10³ 10⁴ 10⁵
Cr ppm